Geophysical Journal International

Geophys. J. Int. (2022) **231,** 1233–1251
Advance Access publication 2022 June 22
GJI Seismology

https://doi.org/10.1093/gji/ggac232

Measuring the phase of ambient noise cross correlations: anisotropic Rayleigh and Love wave tomography across the Oman Mountains

L. Wiesenberg [1], C. Weidle [1], A. El-Sharkawy,[1,2,3] M. Timkó,[4] S. Lebedev [5] and T. Meier[1]

[1] *Institute of Geoscience, Christian-Albrechts University,* 24118 *Kiel, Germany. E-mail: lars.wiesenberg@ifg.uni-kiel.de*
[2] *National Research Institute of Astronomy and Geophysics (NRIAG),* 11421 *Helwan, Cairo, Egypt*
[3] *Faculty of Earth Sciences, Beni-Suef University,* 62511 *Beni-Suef, Egypt*
[4] *Institute of Earth Physics and Space Science, Kövesligethy Radó Seismological Observatory,* 1112 *Budapest, Hungary*
[5] *Department of Earth Sciences, University of Cambridge, Cambridge,* CB2 1TN, *UK*

Accepted 2022 June 20. Received 2022 June 9; in original form 2021 October 13

SUMMARY

Ambient seismic noise tomography has, over the last two decades, developed into a well-established tool for imaging seismic properties of the Earth's crust. Fundamental mode Rayleigh and Love wave phase velocity dispersion curves can be measured from ambient noise cross-correlation functions (CCF) either using a high-frequency approximation theory, or by fitting the spectrum of the CCF to a Bessel function. Here, we advance the latter approach and present an automated algorithm that fits the phase of the Hankel function to the phase of the causal symmetric part of the CCF in order to determine phase velocity curves as continuous functions of frequency. Synthetic tests verify the reliability of the proposed method in the presence of low signal-to-noise ratio (SNR). Moreover, usage of the phase allows for robust phase velocity measurements at longer periods than when using the zero crossings of the Bessel function only and is, therefore, particularly useful at short inter-station distances. In the frequency domain, acceptable bandwidths of smooth phase velocity curves are obtained in an automated procedure using a set of fine-tuned quality criteria. We apply the method to 2.5 yr of continuous waveform data recorded by 58 temporary and permanent broad-band seismic stations in northern Oman. We obtain 1072 and 670 phase velocity curves for Rayleigh and Love waves, respectively, in the period range of 2–40 s. The data are inverted for isotropic and azimuthally anisotropic period-dependent phase velocity maps. Synthetic reconstruction tests show that the phase velocity maps have a lateral resolution of ∼30 km. The results suggest distinctly different middle to lower crustal architecture between the northern and eastern Oman Mountains. Azimuthal anisotropy shows contrasting fast propagation orientations in the shallow and deep crust, which we attribute to stress-induced and structural anisotropy in the upper crust and to lattice-preferred orientation in the lower crust.

Key words: Interferometry; Seismic anisotropy; Seismic noise; Seismic tomography; Surface waves and free oscillation; Crustal structure.

1 INTRODUCTION

The potential of using ambient noise tomography (ANT) to obtain Rayleigh and Love wave phase and group velocity maps has been long recognized. The method is successfully applied to construct high-resolution 3-D shear wave (V_s) models on local (e.g. Picozzi *et al.* 2009; Ryberg *et al.* 2016; Stork *et al.* 2018), regional (e.g. Shapiro *et al.* 2005; Yao *et al.* 2006; Gudmundsson *et al.* 2007; Lin *et al.* 2008; Kästle *et al.* 2016, 2018) and continental scales (e.g. Yang *et al.* 2007; Bensen *et al.* 2008; Ekström *et al.* 2009; Li *et al.* 2010). At regional scales, it enables surface wave measurements at relatively short periods (<5–30 s) along inter-station paths (e.g. Shapiro & Campillo 2004; Sabra *et al.* 2005; Shapiro *et al.* 2005; Yao *et al.* 2006; Bensen *et al.* 2007; Lin *et al.* 2008; Fry *et al.* 2010; Verbeke *et al.* 2012; Molinari *et al.* 2015; Kästle *et al.* 2016, 2018). While it is also possible to determine phase velocities at these periods from regional and teleseismic earthquakes (Endrun *et al.* 2004; Meier *et al.* 2004; Soomro *et al.* 2016; El-Sharkawy *et al.* 2020; Bonadio *et al.* 2021), ambient noise wavefields have the advantage that they do not depend on earthquake occurrences and are recorded continuously (Paul *et al.* 2005). This makes surface wave

dispersion measurements from ambient noise cross correlations well suited to investigate Earth structure from the shallow crust down to the uppermost mantle.

Both theoretical considerations (Weaver & Lobkis 2001; Snieder 2004; Wapenaar 2004; Roux *et al.* 2005; Sánchez-Sesma & Campillo 2006; Fichtner & Tsai 2019) and experimental evidence (Lobkis & Weaver 2001; Derode *et al.* 2003; Larose *et al.* 2005) indicate that ambient noise cross-correlation functions (CCF) of a diffuse or equipartitioned surface wavefield can be used to analyse surface wave propagation between a considered station pair. Using the stationary-phase approximation, Snieder (2004) showed that cross correlating the continuously recorded seismic noise implicitly cancels out the contribution of sources that are not aligned with the station–station azimuth. Lobkis & Weaver (2001), Weaver & Lobkis (2004) and Sánchez-Sesma & Campillo (2006) found that a full reproduction of the Green's function requires a fully diffuse wavefield and stationary noise sources. In practice, these conditions are not generally met. The ambient noise wavefield at any frequency is excited by heterogeneously distributed and non-stationary sources (e.g. Stehly *et al.* 2006; Ermert *et al.* 2016; Juretzek & Hadziioannou 2016) and noise cross correlations are sensitive to the azimuthal distribution of the sources as well as the source–receiver distances. Thus, the reconstructed Green's functions are degenerated (Halliday & Curtis 2008; Tsai 2009; Fichtner 2014, 2015; Stehly & Boué 2017). Nevertheless, the CCFs themselves can still be used to estimate phase and group velocities (Cupillard & Capdeville 2010; Froment *et al.* 2010; Tsai & Moschetti 2010) for Rayleigh and Love waves.

Different approaches have been developed to measure phase and group velocities (e.g. Bensen *et al.* 2007; Gouedard *et al.* 2008; Lin *et al.* 2008; Ekström *et al.* 2009; Tsai 2009) in both time and frequency domain. These approaches are based on the pioneering studies by Aki (1957) and Claerbout (1968). Most time-domain approaches rely on the far-field approximation (e.g. Lin *et al.* 2008; Yao & Van Der Hilst 2009; Luo *et al.* 2015) and assume that time-domain cross correlations can be utilized to estimate group velocity dispersion curves at discrete periods (e.g. via the Frequency–Time Analyses, FTAN, Dziewonski *et al.* 1969; Ritzwoller & Levshin 1998; Levshin *et al.* 2012). Tsai (2009) introduced a framework to quantify possible errors due to anisotropic noise source distribution or non-uniform velocity structures by evaluating the CCF at positive times via the Bessel and Struve function. Fry *et al.* (2010) and Verbeke *et al.* (2012) applied the two-station method of Meier *et al.* (2004) to the ambient noise CCF and estimated phase velocities from its phase.

Based on the spectral analysis of stochastic waves from stationary random processes, Aki (1957) found that the normalized cross-spectrum at two stations varies like a zero-order Bessel function that depends on the frequency-dependent seismic velocity and inter-station distance. Ekström *et al.* (2009) utilized the original work of Aki (1957) and developed an algorithm to extract phase velocity measurements at discrete frequencies by associating the zero crossings of the real part cross-spectrum with the zeros of the Bessel function. They treated the zero crossings of different polarity separately (positive-to-negative and negative-to-positive) to obtain robust phase velocity measurements. Kästle *et al.* (2016) used the zero-crossing approach and included a correction term for Love wave phase velocities which is based on Aki (1957) and particularly relevant for longer periods. Limitations of the zero-crossing method include its imperfect ability to deal with small inter-station distances, since only a few zero crossings may occur. This limits, in particular, the longer period end of the obtained dispersion curves. Spurious zero crossings due to low signal-to-noise ratio (SNR) may also lead to erroneous determination of phase velocities and require smoothing of the cross-spectrum which enhances the robustness of the phase velocity curves (e.g. Ekström *et al.* 2009; Kästle *et al.* 2016). Menke & Jin (2015) used waveform fitting in order to estimate frequency-dependent phase velocities from the ambient noise cross-spectra at low SNR.

In this paper, we present a new automated algorithm for the measurement of Rayleigh and Love wave phase velocities from ambient noise cross correlations. After applying a filtering and weighting scheme, the phase of the Hankel function is matched to the phase of the CCFs causal symmetric part, so as to determine phase velocities as a continuous function of frequency. We start with theoretical considerations and synthetic examples to describe and validate the method and compare different approximations of the imaginary part of the causal symmetric part of the CCF. We then apply it to a regional data set recorded across the Oman Mountains at the eastern Arabian continental margin (Weidle *et al.* 2013). The resulting phase velocity dispersion curves in the period range of 2–40 s are finally inverted for isotropic and azimuthally anisotropic phase velocity maps which provide for the first time insight into the structure of the heterogeneous eastern Arabian continental crust.

2 DATA SET AND AMBIENT NOISE CROSS CORRELATION

We operated a seismic network of 40 broad-band seismic stations in the area of northern Oman from October 2013 to February 2016 (Weidle *et al.* 2013). The network involved thirty Güralp CMG-3ESP Compact, six Trillium 120 PA and four STS-2 seismometers, all equipped with an EarthData PR6-24 Logger as a recording unit. About 2.5 yr of continuously recorded waveforms have been collected with a sampling rate of 100 Hz. The data set is more than 90 per cent complete and only one station (COO35) required data correction due to time synchronization problems. It was complemented by continuous recordings from 18 local permanent seismic stations, operated by the Earthquake Monitoring Center Oman (13 stations), the Dubai Seismic Network (4 stations) and the Global Seismic Network (1 station). While processing the data, a wrong polarity of the continuous data of station FAQ from the Dubai Seismic Network was detected which we corrected for our purposes.

Fig. 1 shows the station distribution across the area ($\sim$500 $\times$ 150 km^2) with an average inter-station distance of $\sim$100 km. The deployed network covers the Semail ophiolite, the largest and best-preserved oceanic lithosphere on land that has been obducted on top of the passive Arabian margin in Late Cretaceous (e.g. Nicolas & Boudier 2011). The collected data set provides a profound basis for illuminating the properties of the eastern Arabian continental crust.

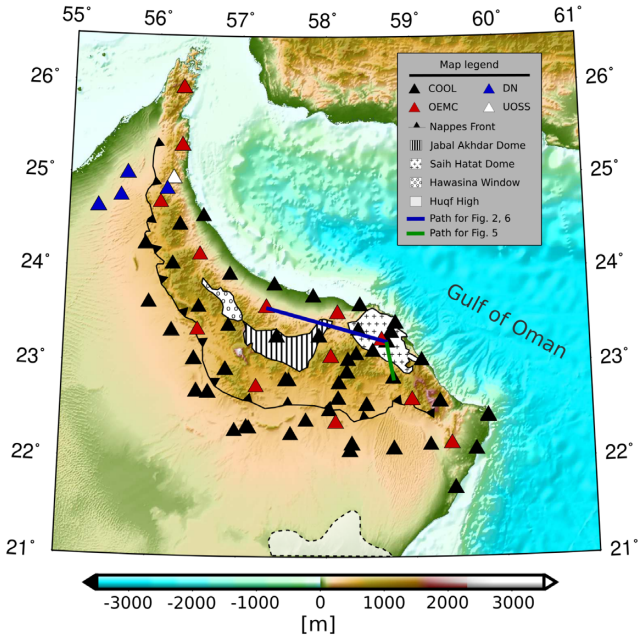

Figure 1. Distribution of seismic stations across northern Oman. Black triangles indicate the location of the temporary stations from the COOL network (Weidle *et al.* 2013), whereas red ones show the locations of local permanent stations from Earthquake Monitoring Center Oman. Locations of complementary stations from the Dubai Seismic Network as well as the Global Seismic Network are indicated by blue and white triangles, respectively. Tectonic features across the Oman Mountains are modified from Nicolas & Boudier (2011) and Oterdoom *et al.* (1999).

We compute CCFs following mainly the approach described by Bensen *et al.* (2007). Raw continuous seismic data are cut into daily segments and downsampled to 5 Hz. The daily segments are demeaned, detrended and corrected for the instrument responses. To suppress transient signals (i.e. phases from teleseismic earthquakes and local or instrumental transients), a running absolute mean normalization in the time domain and whitening in the frequency domain are applied to the data (Bensen *et al.* 2007). Daily cross correlations are then estimated between all possible station combinations. To improve the SNR of surface wave signals, stacking of the daily CCF is performed. In the lower panel of Fig. 2, we show for a WNW-ESE oriented station-pair (COO02–HOQ, see Fig. 1 for location) the temporal stability of the daily CCF for vertical (c) and transverse (d) components. Although both the causal (positive lagtimes, W to E propagation) and the acausal (negative lagtimes, E to W propagation) parts of the CCFs are easily recognized through the seasons, the acausal part is overall stronger. This suggests that noise sources are most of the year dominant in the Indian Ocean but in the (northern hemisphere) winter months the acausal amplitudes degrade and causal amplitudes increase, in line with noise sources in the North Atlantic (e.g. Hillers *et al.* 2012). Despite the amplitude fluctuations over time and from causal to acausal through the seasons, we do not observe measurable changes in the lagtime and therefore stack and average the causal and acausal parts to obtain a single sided symmetric CCF for each station pair.

In the upper panels of Fig. 2, the stacked, symmetric part of the CCF, its time-period representation (Dziewonski *et al.* 1969; Meier *et al.* 2004) and amplitude spectrum are shown for the (a) vertical and the (b) transverse components for the same station pair. The group arrival times of the fundamental modes clearly emerge as a ridge across the time-period map that can be traced in a broad period range (2–64 s) for Rayleigh waves. For Love waves, a complicated pattern at periods shorter than 8 s is observed, which reflects more high-frequency noise in the daily CCFs on the transverse component.

Ambient noise CCFs are calculated for the vertical and transverse components from 2113 possible station combinations in a frequency range of 0.5–100 s. The double-sided stacked CCFs for the vertical (left) and transverse (right) components as a function of inter-station distance and low-pass filtered at 7 s are shown in Fig. 3. They show a clear indication for the Rayleigh and Love wave fundamental modes, whose arrival time increases linearly with inter-station distance (Fig. 3). At long distances (>300 km), Rayleigh wave fundamental modes show higher amplitudes on the acausal parts than on its causal parts. On the other hand, due to low SNR the amplitude of the Love wave are obscured at the same distances.

3 DETERMINATION OF AMBIENT NOISE PHASE VELOCITIES

In this section, we discuss theoretical aspects of our implementation and introduce an automated algorithm for measuring Rayleigh and Love wave phase velocities from the phase of the vertical and transverse components of the CCFs, respectively.

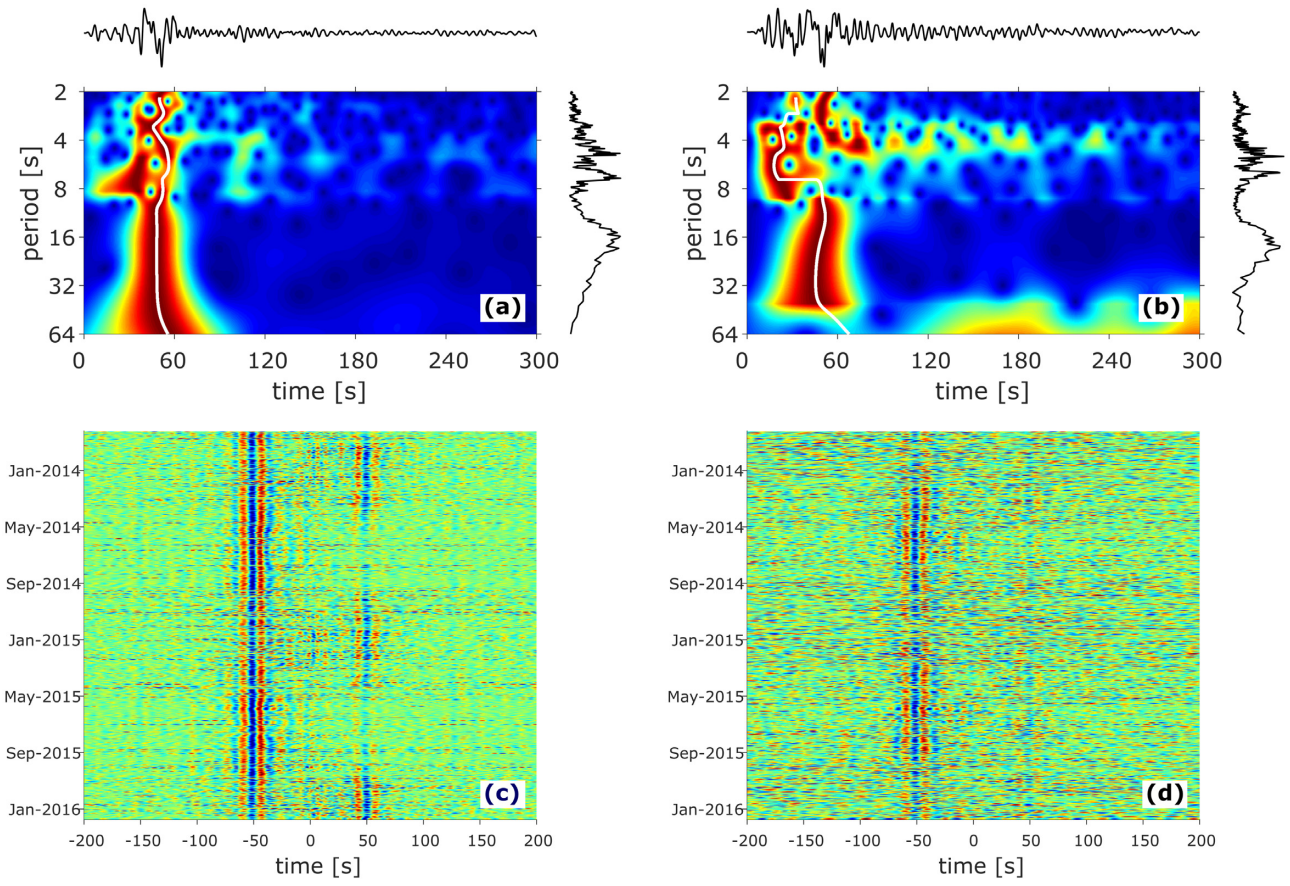

Figure 2. Ambient noise cross correlation for (a, c) the vertical and (b, d) transverse components for the inter-station path COO02–HOQ (for location see Fig. 1). Top panels show the time-period representation after Dziewonski *et al.* (1969) and Meier *et al.* (2004). The stacked CCF in time domain is shown on top and its amplitude spectrum as a function of period on the right-hand side. The white line within the time period representation indicate the group traveltime. Bottom panels show the daily double-sided CCFs of the entire data set recorded by the same path.

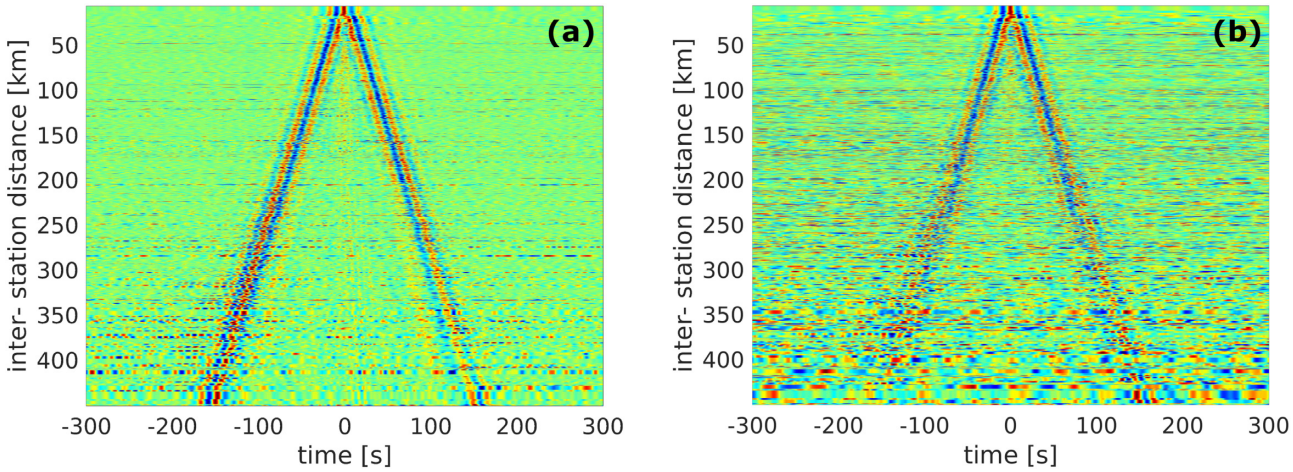

Figure 3. Stacked CCFs for (a) the vertical and (b) transverse components, shown as a function of inter-station distance and low-pass filtered at period of 7 s.

3.1 Rayleigh waves

Ambient noise on the vertical component is assumed to be dominated by fundamental Rayleigh modes from sources located at the surface at large distance from the stations (Halliday & Curtis 2008). The far-field displacement of the Rayleigh wave in the frequency domain at station j is given by, for example, Aki & Richards (2002):

$$u_j(\omega) = A(\omega)e^{i\phi_0(\omega)}\sqrt{\frac{2c(\omega)}{\pi\omega r_j}}e^{-i\left(\frac{\omega r_j}{c(\omega)}+\frac{\pi}{4}\right)}, \quad (1)$$

where $A(\omega)$ and $\phi_0(\omega)$ represent the amplitude and phase spectra of the source, ω is the angular frequency, $c(\omega)$ is the phase velocity and r_j indicates the distance travelled from the source to the receiver j. Accordingly, the vertical component of the CCF for a single ambient noise source recorded at two stations can be expressed as:

$$\rho_{u_1u_2}(\omega) = A^2(\omega)\frac{2c(\omega)}{\pi\omega}\frac{1}{\sqrt{r_1 r_2}}e^{i\frac{\omega}{c(\omega)}(r_1-r_2)} \tag{2}$$

For distant sources, $r_1 - r_2$ can be approximated by the inter-station distance (Δ). Thus, the stacked CCF for homogeneously distributed sources from all directions can be formulated as (e.g. Weemstra *et al.* 2015):

$$\rho_{u_1u_2}(\omega) = \tfrac{2c(\omega)}{\pi\omega R}\tfrac{1}{2\pi}\int_{-\pi}^{\pi} A^2(\omega,\theta)e^{i\frac{\omega\Delta}{c(\omega)}\cos(\theta)}d\theta \tag{3}$$

$$= \tfrac{2c(\omega)}{\pi\omega R}A^2(\omega)J_0\left(\tfrac{\omega\Delta}{c(\omega)}\right), \tag{4}$$

where θ represents the angle towards the source. R indicates the radius of the great circle connecting the two receivers. J_0 denotes the Bessel function of first kind (Aki 1957). It describes the dispersive properties of the CCF caused by the fundamental Rayleigh mode travelling from one station to another and vice versa, assuming that the noise wavefield is isotropic (i.e. $A(\omega)$ is independent of θ). In this case, the CCF is a symmetric function in the time domain and thus the spectrum is consequently real valued that allows to measure phase velocities, for example, by evaluating the zero crossings (e.g. Ekström *et al.* 2009; Ekström 2017; Boschi *et al.* 2012; Kästle *et al.* 2016) or waveform fitting (Menke & Jin 2015). Although eq. (4) is a highly useful analytic expression for the ambient noise CCF, the non-zero value of the Bessel function at frequency zero is non-physical if distant sources are considered (see Fig. S1a in the Supporting Information). In practice, windowing and tapering around the fundamental mode surface wave in the time-domain results in a 'tapered' CCF spectrum at low frequencies, as long periods are removed from the time-series (Fig. S1c, Supporting Information).

We consider the causal symmetric part of the CCF ($\tilde{\rho}_{u_1u_2}$). Due to non-homogeneous distributions of the ambient noise sources, the observed CCF is usually non-symmetric (Fig. 2). The causal symmetric, single-sided CCF is therefore approximated by the symmetric part of the observed CCF:

$$\tilde{\rho}_{u_1u_2}(t) = \frac{1}{2}(\rho_{u_1u_2}(t) + \rho_{u_1u_2}(-t)), \quad t \geq 0. \tag{5}$$

The imaginary part of its spectrum is non-zero and is related to the real part of the spectrum by the Hilbert transform ($\mathcal{H}$) (e.g. Nakahara 2006; Sánchez-Sesma & Campillo 2006; Tsai 2009):

$$\tilde{\rho}_{u_1u_2}(\omega) = \frac{c(\omega)}{\pi\omega R}A^2(\omega)\left[J_0\left(\frac{\omega\Delta}{c(\omega)}\right) + i\mathcal{H}\left\{J_0\left(\frac{\omega\Delta}{c(\omega)}\right)\right\}\right]. \tag{6}$$

An analytic approximation of the Hilbert transform of the real part of the spectrum allows to relate the phase of the causal symmetric part of the CCF analytically to the phase velocity of Rayleigh waves. The imaginary part of eq. (6) can be approximated by either the Struve function (S_0) or the Neumann function (Y_0) of zero order (Tsai 2009):

$$\tilde{\rho}_{u_1u_2}(\omega) \approx \tfrac{c(\omega)}{\pi\omega R}A^2(\omega)\left[J_0\left(\tfrac{\omega\Delta}{c(\omega)}\right) + iY_0\left(\tfrac{\omega\Delta}{c(\omega)}\right)\right] = \tfrac{c(\omega)}{\pi\omega R}A^2(\omega)H_0^{(1)}\left(\tfrac{\omega\Delta}{c(\omega)}\right) \tag{7}$$

$$\approx \tfrac{c(\omega)}{\pi\omega R}A^2(\omega)\left[J_0\left(\tfrac{\omega\Delta}{c(\omega)}\right) + iS_0\left(\tfrac{\omega\Delta}{c(\omega)}\right)\right], \tag{8}$$

where eq. (7) is proportional to the Hankel function of first kind ($H_0^{(1)}$). Please note that we use here S_0 for the Struve function instead of H_0 as common in the literature (e.g. Abramowitz & Stegun 1964; Tsai 2009) for clarity. The phase of the causal symmetric part of the CCF is a function of Rayleigh wave phase velocity and can therefore be evaluated from either eqs (6)–(8):

$$\phi_R(\omega) = a\tan\left(\frac{\mathcal{H}\left\{J_0\left(\frac{\omega\Delta}{c_R(\omega)}\right)\right\}}{J_0\left(\frac{\omega\Delta}{c_R(\omega)}\right)}\right), \tag{9}$$

$$\phi_{Y,R}(\omega) = a\tan\left(\frac{Y_0\left(\frac{\omega\Delta}{c_{Y,R}(\omega)}\right)}{J_0\left(\frac{\omega\Delta}{c_{Y,R}(\omega)}\right)}\right), \tag{10}$$

$$\phi_{S,R}(\omega) = a\tan\left(\frac{S_0\left(\frac{\omega\Delta}{c_{S,R}(\omega)}\right)}{J_0\left(\frac{\omega\Delta}{c_{S,R}(\omega)}\right)}\right). \tag{11}$$

Here, $\phi_R(\omega)$ and $c_R(\omega)$ represent the exact phase and phase velocity of the spectrum as defined by the Hilbert transform of the real part (eq. 6). $\phi_{Y,R}(\omega)$ is the phase approximated by the Neumann function as the imaginary part (eq. 7) which depends on its phase velocity $c_{Y,R}(\omega)$. $\phi_{S,R}(\omega)$ and $c_{S,R}(\omega)$ are the phase and phase velocity approximated by the Struve function as the imaginary part of the causal symmetric part of the CCF. The differences between the phase velocities determined using either the Neumann or Struve function as imaginary parts are negligible at high frequencies due to the similarity of Y_0 and S_0 for large arguments (Abramowitz & Stegun 1964; Tsai 2009, see Fig. S1, Supporting Information). At low frequencies, however, both phase velocities are different due to different behaviour of Y_0 and S_0 for small arguments. Specifically, S_0 is a better representation of the Hilbert transform of J_0 than Y_0. However, careful tapering of the spectrum at low frequencies practically removes the phase difference determined using either the Neumann and the Struve function as imaginary parts (Fig. S1d, Supporting Information).

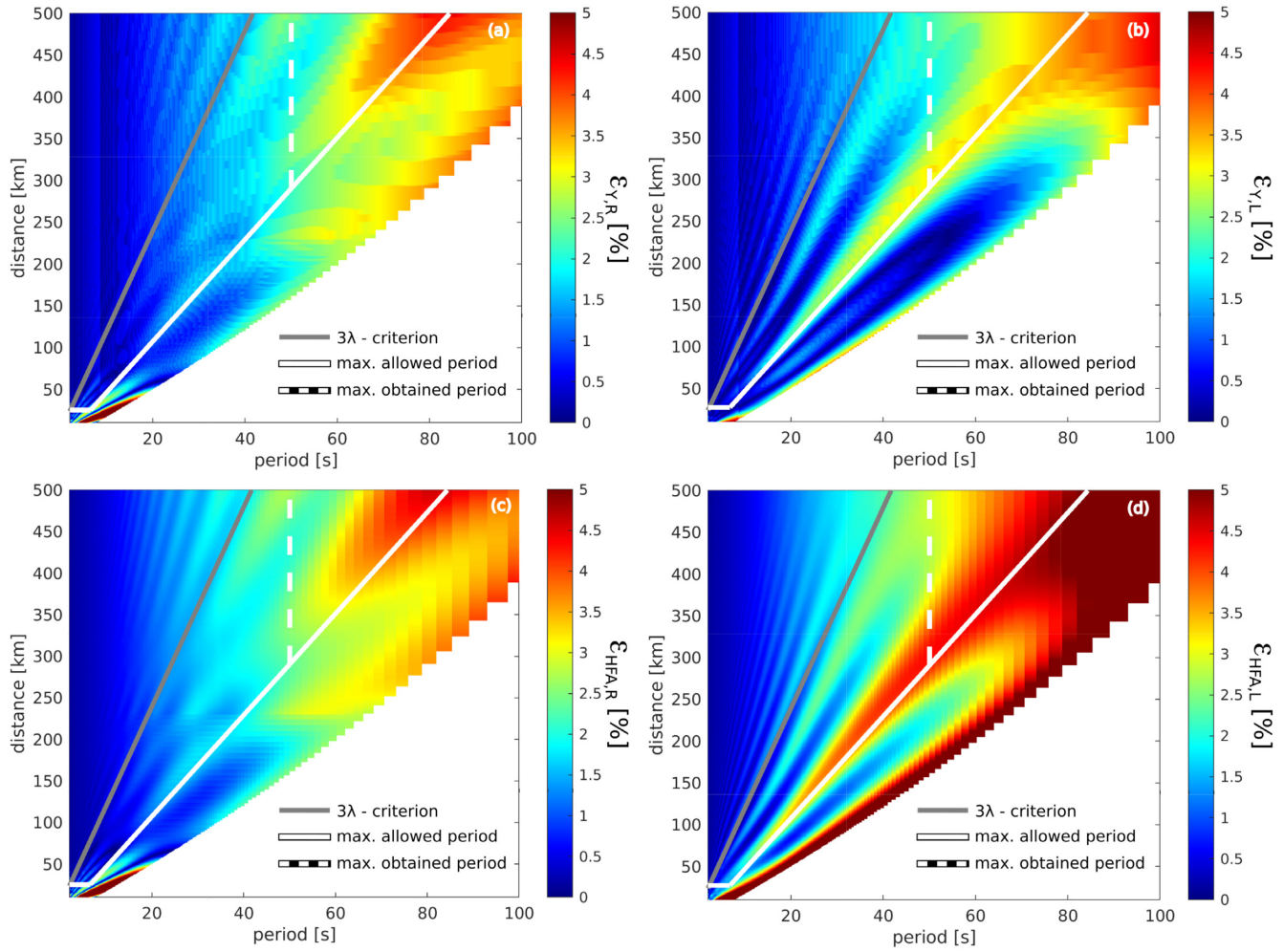

Figure 4. Error estimation ($\varepsilon(\omega, \Delta)$) in the phase velocities using (a, b) the Hankel function and (c, d) the high-frequency approximation, respectively as a function of period and inter-station distance for both (a, c) Rayleigh and (b, d) Love waves. Actual phases are estimated using the Hilbert transform on phase velocities synthesized from PREM (Dziewonski & Anderson 1981) for all cases. The grey line shows the three-wavelength criterion following Bensen *et al.* (2007). The white line indicate the limit of the maximum allowed period as a function of inter-station distance from our measurement procedure described in Section 3.3. The dashed white line shows the maximum obtained period from our data set.

We synthesize phase velocities from the Preliminary Reference Earth Model (PREM, Dziewonski & Anderson 1981) and compute the error $\varepsilon_{Y,R}(\omega, \Delta)$ between actual phase velocities (c_R) and $c_{Y,R}$ using the approximation of the imaginary part by the Neumann function (eq. 10):

$$\varepsilon_{Y,R}(\omega, \Delta) = \frac{c_{Y,R}(\omega) - c_R(\omega)}{c_R(\omega)} \times 100 \text{ per cent.} \tag{12}$$

Fig. 4(a) shows this difference as function of period and inter-station distance. For small periods, the measurement error is overall small and errors increase generally with period. This increase is also strongly dependent on inter-station distance where longer periods can be in principle measured at longer inter-station distances. The 3λ criterion, a cut-off of the maximum allowed period based on the seismic wavelength λ (Bensen *et al.* 2007), is a widely used measure to limit the bandwidth of phase velocity dispersion measurements. Fig. 4(a) shows that the criterion ensures small errors for the Hankel function approximation. However, uncertainties related to the approximation remain also low for longer periods over a wide range of inter-station distances. Thus, the 3λ criterion may be relaxed to longer periods and we note that a long-period cut-off has been implemented variably in the past (e.g. two, Yao & Van Der Hilst 2009 or one λ, Wang *et al.* 2017). In our measurement procedure (Section 3.3), we impose a limit as function of inter-station distance (white line in Fig. 4). We note that besides errors due to the approximation of the ambient noise cross correlation, also a spatial non-homogeneous distribution of noise sources may contribute to measurement errors especially for longer periods and short paths (e.g. Yao & Van Der Hilst 2009; Lin *et al.* 2013). From Fig. 4(a), it is obvious that our limits are more strict than required if only errors in the approximation of the ambient noise cross correlation are considered accounting thus also for possible errors due to a non-homogeneous source distribution. Furthermore, we apply a time–frequency-dependent weighting scheme to carefully smooth the spectrum and to downweight contaminations from body waves, higher mode, and noise, and we

apply very strict quality checks of the dispersion curves (Section 3.3). At large inter-station distances (>300 km), the longest period that we consider in our data is 50 s (white dashed line in Fig. 4) to ensure small errors due to the chosen approximation.

The high-frequency approximation of eq. (3) leads to (Snieder 2004; Boschi & Weemstra 2015):

$$\rho_{u_1u_2}(\omega) \approx \frac{c(\omega)}{\pi\omega R}\left[A^2(\omega,0)\sqrt{\frac{2\pi}{\frac{\omega\Delta}{c(\omega)}}}e^{i\left(\frac{\omega\Delta}{c(\omega)}-\frac{\pi}{4}\right)} + A^2(\omega,\pi)\sqrt{\frac{2\pi}{\frac{\omega\Delta}{c(\omega)}}}e^{-i\left(\frac{\omega\Delta}{c(\omega)}-\frac{\pi}{4}\right)}\right], \tag{13}$$

where $\theta = 0, \pi$ are the stationary points for the stacked CCF describing the high-frequency approximation of the Hankel functions of first and second kind (Boschi & Weemstra 2015). They are often referred to as the causal and acausal part of the stacked CCF. Therefore, the causal part of the CCF of the high-frequency approximation can be approximated as:

$$\tilde{\rho}_{u_1u_2}(\omega) \approx \frac{c(\omega)}{\pi\omega R}A^2(\omega)\sqrt{\frac{2\pi}{\frac{\omega\Delta}{c(\omega)}}}e^{-i\left(\frac{\omega\Delta}{c(\omega)}-\frac{\pi}{4}\right)}. \tag{14}$$

The measured phase $\phi(\omega)$ is therefore in the high-frequency approximation:

$$\phi(\omega) \approx -\frac{\omega\Delta}{c(\omega)} + \frac{\pi}{4} \tag{15}$$

According to eq. (15), a phase shift of $-\pi/4$ has to be applied to the measured phase to obtain a phase velocity estimate $c_{\mathrm{HFA}}(\omega)$:

$$\phi_{\mathrm{HFA}}(\omega) = \phi(\omega) - \frac{\pi}{4} = -\frac{\omega\Delta}{c_{\mathrm{HFA}}(\omega)} \tag{16}$$

$$c_{\mathrm{HFA}}(\omega) = -\frac{\omega\Delta}{\phi_{\mathrm{HFA}}(\omega)}, \tag{17}$$

where $\phi_{\mathrm{HFA}}(\omega)$ is the phase of the CCF corrected according to the high-frequency approximation. At long periods and short inter-station distances, the high-frequency approximation introduces an error to the true phase velocity $c_R(\omega)$ (Fig. 4c). This error $\varepsilon_{\mathrm{HFA},R}(\omega, \Delta)$ can be quantified as:

$$\varepsilon_{\mathrm{HFA},R}(\omega,\Delta) = \frac{c_{\mathrm{HFA}}(\omega) - c_R(\omega)}{c_R(\omega)} \times 100 \text{ per cent}. \tag{18}$$

The error distribution (Fig. 4c) strongly resembles that from using $c_{Y,R}$ above. Detailed inspection in the distance-period range of interest shows that especially at shortest periods, the differences are practically the same. At larger periods of 20–50 s, $c_{Y,R}$ provides slightly smaller errors (≈0.2 per cent) than c_{HFA}. Following our limit for the maximum allowed period, these differences in error increase to 0.5 per cent at periods longer than 60 s and inter-station distance >400 km.

3.2 Love waves

Following Aki & Richards (2002), the Love wave displacement at a horizontal component of station j is given as:

$$u_j(\omega) = A(\omega)e^{i\phi_0(\omega)}\sqrt{\frac{2c(\omega)}{\pi\omega r_j}}e^{-i\left(\frac{\omega r_j}{c(\omega)}+\frac{\pi}{4}\right)}\cos(\theta), \tag{19}$$

where the term $\cos(\theta)$ accounts for the different polarization of the horizontal wave displacement. The stacked transverse component of the CCF of homogeneously distributed noise sources can be expressed as:

$$\begin{aligned}\rho_{u_1u_2}(\omega) &\approx \frac{2c(\omega)}{\pi\omega R}\frac{1}{2\pi}A^2(\omega)\int_{-\pi}^{\pi}e^{i\frac{\omega\Delta}{c(\omega)}\cos(\theta)}\cos^2(\theta)d\theta,\\ &= \frac{c(\omega)}{\pi\omega R}\frac{1}{2\pi}A^2(\omega)\left[\int_{-\pi}^{\pi}e^{i\frac{\omega\Delta}{c(\omega)}\cos(\theta)}d\theta + \int_{-\pi}^{\pi}e^{i\frac{\omega\Delta}{c_L(\omega)}\cos(\theta)}\cos(2\theta)d\theta\right],\\ &\approx \frac{c(\omega)}{\pi\omega R}A^2(\omega)\left[J_0\left(\frac{\omega\Delta}{c(\omega)}\right) - J_2\left(\frac{\omega\Delta}{c(\omega)}\right)\right],\end{aligned} \tag{20}$$

where J_2 is the Bessel function of first kind and second order (Aki 1957; Haney *et al.* 2012). The contribution of the J_2 term might not be neglected at long periods and short inter-station distances (Kästle *et al.* 2016). As for Rayleigh waves, the spectrum of the Bessel functions needs to be tapered carefully at low frequencies. The causal symmetric part of the CCF introduces an imaginary part which is related to the real part by the Hilbert transform:

$$\tilde{\rho}_{u_1u_2}(\omega) = \frac{c(\omega)}{2\pi\omega R}A^2(\omega)\left[\left[J_0\left(\frac{\omega\Delta}{c(\omega)}\right) - J_2\left(\frac{\omega\Delta}{c(\omega)}\right)\right] + i\mathcal{H}\left\{\left[J_0\left(\frac{\omega\Delta}{c(\omega)}\right) - J_2\left(\frac{\omega\Delta}{c(\omega)}\right)\right]\right\}\right]. \tag{21}$$

The imaginary part can be approximated by the Neumann functions of zero (Y_0) and second order (Y_2):

$$\tilde{\rho}_{u_1u_2}(\omega) \approx \frac{c(\omega)}{2\pi\omega R}A^2(\omega)\left[\left[J_0\left(\frac{\omega\Delta}{c(\omega)}\right) - J_2\left(\frac{\omega\Delta}{c(\omega)}\right)\right] + i\left[Y_0\left(\frac{\omega\Delta}{c(\omega)}\right) - Y_2\left(\frac{\omega\Delta}{c(\omega)}\right)\right]\right]. \tag{22}$$

$$\approx \frac{c(\omega)}{2\pi\omega R} A^2(\omega)\left[H_0^{(1)}\left(\frac{\omega\Delta}{c(\omega)}\right) - H_2^{(1)}\left(\frac{\omega\Delta}{c(\omega)}\right)\right], \tag{23}$$

where $H_0^{(1)}$ and $H_2^{(1)}$ represent the Hankel function of first kind of the zero and the second orders, respectively. The phase of the transverse component causal symmetric part of the CCF is a function of Love wave phase velocity and therefore be evaluated from either eq. (21) or (22):

$$\phi_L(\omega) = a\tan\left(\frac{\mathcal{H}\left\{J_0\left(\frac{\omega\Delta}{c_L(\omega)}\right) - J_2\left(\frac{\omega\Delta}{c_L(\omega)}\right)\right\}}{J_0\left(\frac{\omega\Delta}{c_L(\omega)}\right) - J_2\left(\frac{\omega\Delta}{c_L(\omega)}\right)}\right), \tag{24}$$

$$\phi_{Y,L}(\omega) = a\tan\left(\frac{Y_0\left(\frac{\omega\Delta}{c_{Y,L}(\omega)}\right) - Y_2\left(\frac{\omega\Delta}{c_{Y,L}(\omega)}\right)}{J_0\left(\frac{\omega\Delta}{c_{Y,L}(\omega)}\right) - J_2\left(\frac{\omega\Delta}{c_{Y,L}(\omega)}\right)}\right), \tag{25}$$

where $\phi_L(\omega)$ is the exact phase estimated from the Hilbert transform (eq. 21) which depends on the phase velocity $c_L(\omega)$. $\phi_{Y,L}(\omega)$ and $c_{Y,L}(\omega)$ are the phase and phase velocity approximated by the Neumann functions as the imaginary part of the causal symmetric part of the CCF.

The difference between the Love wave phase velocity obtained from the phase of the Hankel function (eq. 25) and the true phase velocity (Fig. 4b) are slightly larger than for Rayleigh waves. It is quantified as:

$$\varepsilon_{Y,L}(\omega, \Delta) = \frac{c_{Y,L}(\omega) - c_L(\omega)}{c_L(\omega)} \times 100 \text{ per cent.} \tag{26}$$

However, the 3λ criterion is still conservative. We note that for Love waves, the Struve function is a poor approximation of the Hilbert transform of the real part because of the presence of the additional J_2 term.

In the high frequency limit, J_2 approaches zero (Kästle *et al.* 2016). Similar to Rayleigh waves, thus Love wave phase velocities can be measured using the high frequency approximation (eq. 17). The error to the true phase velocity $c_L(\omega)$ is:

$$\varepsilon_{\mathrm{HFA},L}(\omega, \Delta) = \frac{c_{\mathrm{HFA}}(\omega) - c_L(\omega)}{c_L(\omega)} \times 100 \text{ per cent.} \tag{27}$$

At long periods and small inter-station distances, errors in Love phase velocities using the high-frequency approximation are much larger compared to Rayleigh waves (Fig. 4d). Since the phase velocity calculations are the same for Rayleigh and Love waves in the high-frequency approximation (Kästle *et al.* 2016), the larger error can be related to the contribution of the J_2 term to $c_L(\omega)$ for Love waves. The high-frequency approximation provides phase velocities of similar accuracies as $c_{Y,L}$ at shortest periods. However, errors are on average 0.6 per cent larger at periods of 20–50 s and of more than 1.2 per cent for periods larger than 75 s and large inter-station distances.

3.3 Automated selection of the phase velocity dispersion curves

Rayleigh and Love wave phase velocity dispersion curves are calculated from the filtered and weighted phases of the CCF in the frequency domain following an adopted version Meier *et al.* (2004) and Soomro *et al.* (2016). Initial phase velocity estimates from the high-frequency approximation (eq. 17) are gradually changed till their phases, calculated from the Hankel function match the measured phases of the CCF. Due to the inherent 2π ambiguity of the measured phase, we obtain a bundle of phase velocity curves.

Synthetic as well as real data tests are performed to compare phase velocities obtained from the phase as described above and from evaluation of the zeros of the Bessel function (Fig. 5). The real part of the spectrum of the CCF as well as the corresponding phase velocities for both the synthetic and real data cases calculated from the unfiltered CCF are shown in Figs 5(a) and (b), respectively. A local CRUST1.0 model (Laske *et al.* 2013) and eq. (9) are used to construct a synthetic phase as a function of frequency for an inter-station distance of 43 km. The resulting spectrum yields the synthetic CCF in the time domain which will be contaminated by 2 per cent of random noise. For the real data test, a CCF calculated at an inter-station distance of 43 km is considered. Comparison of the raw, unfiltered spectra (Figs 5a and b) shows that the amplitude at lowermost frequencies is indeed 'tapered' in reality, underlining the significance of taking tapering into account in the theoretical discussion above. The figure also shows that despite of the method, it will become difficult to obtain robust phase velocities from the raw spectra if the SNR is low. Also note, that the spectral sampling of zeros is strongly distance dependent and fewer zeros are available for phase velocity measurements at short inter-station paths. Despite the low SNR in Figs 5(a) and (b), using the phase would still allow to extract a rough continuous dispersion curve without 2π jumps, whereas evaluation of zeros requires an additional procedure that fixes phase jumps due to spurious zero crossings. This can be achieved, for example, by varying the number of missed or added zero crossings (Fig. 5c) to obtain different phase velocity curves based on a regional background model (Ekström *et al.* 2009).

To reduce the roughness of the phase in the raw spectra and derive a smooth dispersion curve, the spectrum is typically smoothed prior to phase velocity measurements (e.g. Ekström *et al.* 2009). Here, we apply the spectral filtering and weighting scheme of Meier *et al.* (2004) and Soomro *et al.* (2016). This allows for robust phase velocity measurements from both methods (Figs 5c and d). Smoothing of the spectrum also reduces the effects of a non-uniform noise distribution or undesired local noise sources at small inter-station paths. This allows for an overall relaxation of the 3λ criterion of Bensen *et al.* (2007) and for phase velocity measurements in a wider frequency range. Furthermore, our approach using the phase of the Hankel function yields denser frequency sampling of the phase velocity measurements, even for short inter-station distances of <50 km, that only depends on the length of the CCF. In contrast, only a few zero crossings may occur in the frequency range, decreasing the resolution of the phase velocity curve.

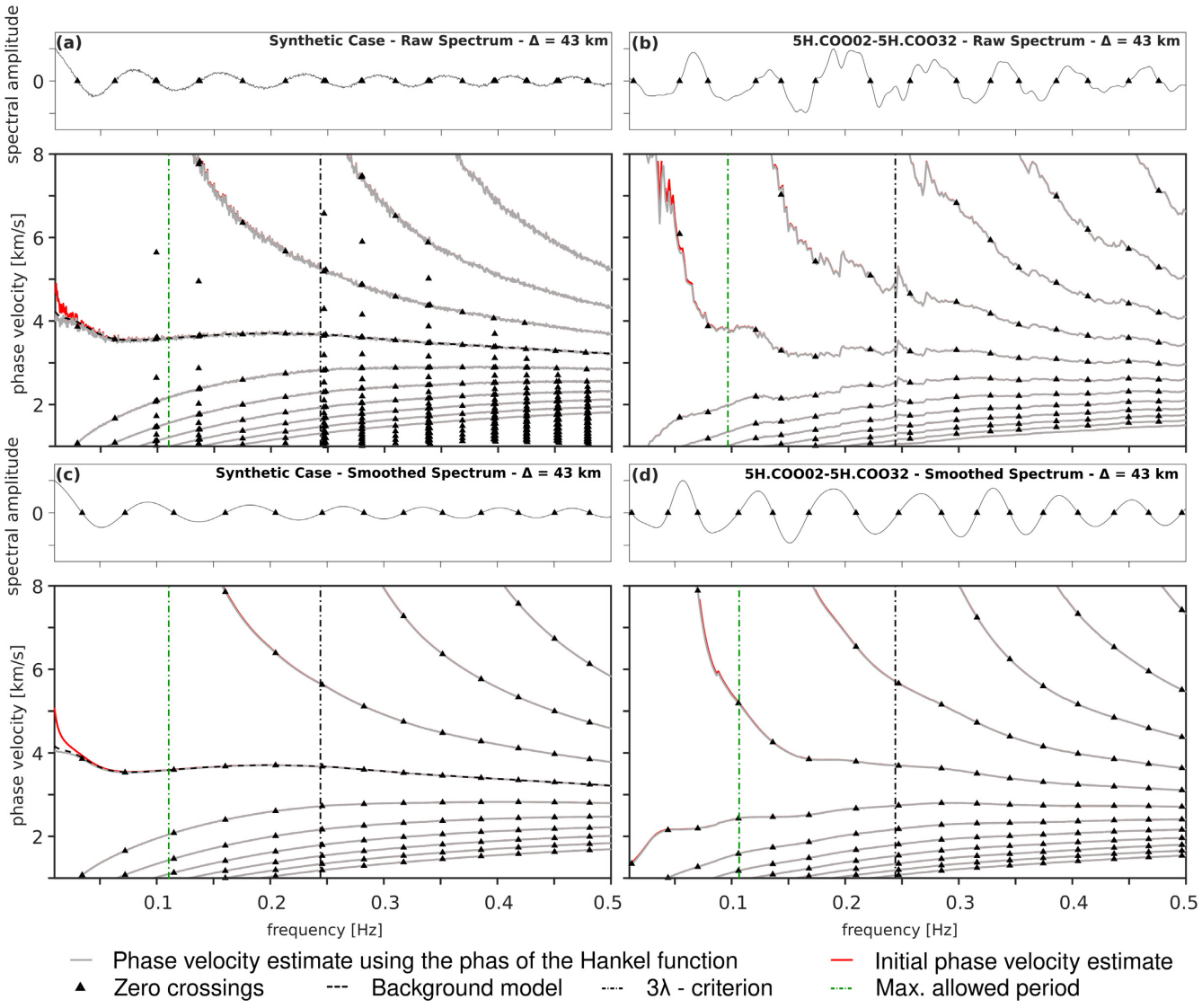

Figure 5. Synthetic and real example of Rayleigh wave phase velocity measurements using the phase of the CCF compared to those from the zero-crossings method. The synthetic CCF was constructed from a CRUST1.0 model (Laske *et al.* 2013) at inter-station distance of 43 km and superimposed by 2 per cent of random noise and the corresponding phase velocity measurements (a) before and (c) after the application of the weighting scheme of Meier *et al.* (2004). The panels from (b) and (d) show the phase velocity measurements from a real data case at 43 km inter-station distance. The black triangles depict locations of the zero crossings in the real part of the spectrum as well as the phase velocity curves from the zero-crossing method. While, the phase velocities from the background model are indicated by a dashed black line, phase velocities from the phase of the CCF using the high-frequency approximation (initial estimate) and those using the phase of the Hankel function are shown in red and grey curves, respectively.

To identify the correct 2π branch and retain smooth phase velocity dispersion curves, we introduce an automated selection procedure based on three main criteria, modified after Soomro *et al.* (2016). These criteria are illustrated in Fig. 6.

(i) *Background model criterion:* the correct phase velocity branch is defined by a direct comparison with phase velocities of a local reference model calculated from CRUST1.0 (Laske *et al.* 2013) at a reference period (Fig. 6a). The maximum allowed deviation from the reference model (grey dashed lines, an empirically defined threshold) vary as function of frequency. While it is kept constant at intermediate and low frequencies ($<$ 100 mHz), we allow the threshold to increase linearly at higher frequencies ($\geq$100 mHz) in order to account for structural heterogeneities from large sedimentary basins and complexities in the shallow crustal layers. The portions of the curve that exceed this threshold are rejected (blue segment in Fig. 6a).

(ii) *Smoothness criterion:* it aims for evaluating the phase velocity perturbations to ensure a certain degree of smoothness on the measured curve. At intermediate and low frequencies ($<$100 mHz), the roughness of each dispersion curve is calculated according to eq. (28). We estimate the first partial derivative of the measured phase velocity ($c'(\omega_j)$) with respect to frequency and compare it with the corresponding value of the reference model ($c'_{\rm ref}(\omega_j)$). Then a summation of the absolute values of the derivative deviation from the reference model over a moving window in the frequency domain is performed (Soomro *et al.* 2016). The absolute value is taken so that positive as well as negative deviations are treated in the same way (Soomro *et al.* 2016). The frequency range of the summation is increasing linearly towards higher

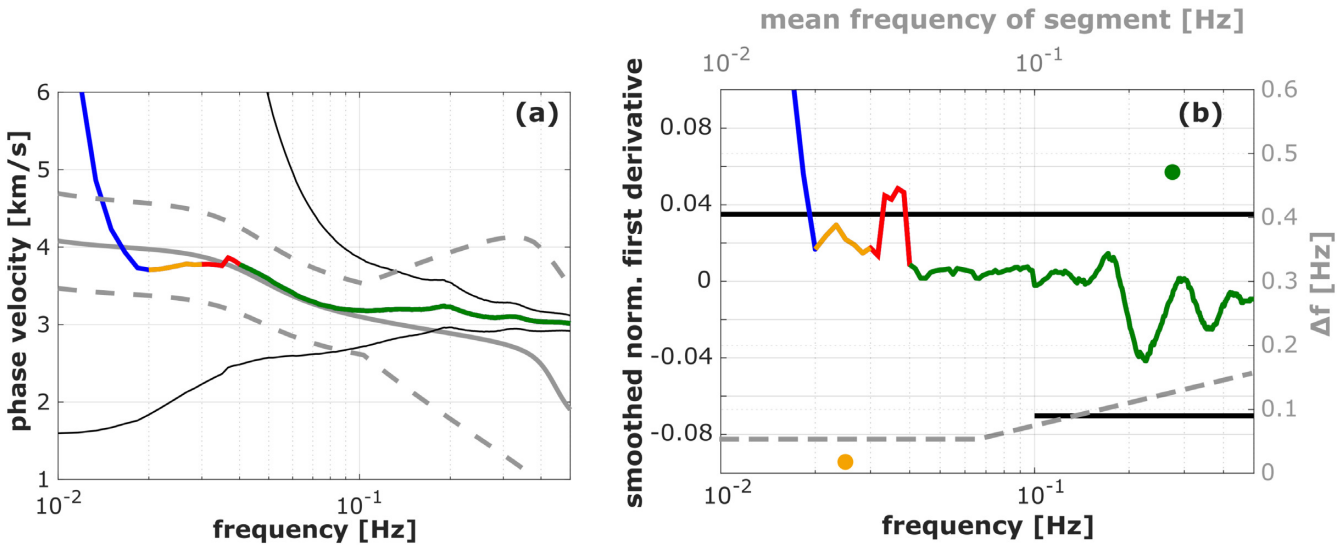

Figure 6. Selection criteria of the automated ambient noise phase velocity measurements, adapted for short periods after Soomro *et al.* (2016). (a) Background model criterion. The grey lines indicate the phase velocities from CRUST1.0 (Laske *et al.* 2013) as well as the maximum deviation thresholds (dashed). The thin black lines indicate the 2π ambiguities of the selected, multicoloured phase velocity branch. (b) Smoothness (black, left y-axis) and length (grey, right y-axis) criteria. The multicoloured curve show the smoothness of the previously selected dispersion curve. The colour coded dots indicate the length of the corresponding segments. Blue and red segments violate against the background model and the smoothness criteria, respectively. Orange segment is rejected due to its length. The green segment of the curve satisfies all selection criteria and is accepted.

frequency, to account for the greater first derivative of the phase velocities. Thus, a frequency independent threshold is applied ($\mathrm{th}_S = 0.035$, horizontal black lines in Fig. 6b). At higher frequencies ($\geq$100 mHz), the roughness of the selected dispersion curve is quantified by exploring relative values of the first derivative of the measured phase velocities only. This can be formulated as:

$$S(\omega_i) = \begin{cases} \sum_{\omega_j=\omega_i-d(\omega_i)}^{\omega_i+d(\omega_i)} \left| \frac{c'(\omega_j) - c'_{ref}(\omega_j)}{c'_{ref}(\omega_j)} \right| \Delta f < \mathrm{th}_S, & \text{for} \quad \omega_i < 100\,\mathrm{mHz} \qquad (28) \\ \sum_{\omega_j=\omega_i-d(\omega_i)}^{\omega_i+d(\omega_i)} c'(\omega_j)\,\Delta f < \mathrm{th}_S, & \text{for} \quad \omega_i \geq 100\,\mathrm{mHz} \qquad (29) \end{cases}$$

The red segment of the curve violates against the smoothness criterion (Fig. 6).

(iii) *The length criterion:* to avoid too short dispersion curves, we apply the length criterion as introduced by Soomro *et al.* (2016). This criterion is frequency-dependent (i.e. relaxed at low frequencies and more stricter at high frequencies). In Fig. 6(b), colour coded dots indicate the length of the corresponding segments of the dispersion curves. The orange segment is rejected due to its short length. The green segment of the dispersion curve satisfies all criteria and is thus accepted.

4 APPLICATION TO NORTHERN OMAN: AZIMUTHALLY ANISOTROPIC PHASE VELOCITY MAPS FROM AMBIENT NOISE TOMOGRAPHY

We applied the method to the COOL data set and obtained 1072 Rayleigh and 663 Love wave phase velocity dispersion curves in the period range from 2 to 40 s (Fig. 7). The number of the measured curves as a function of period for Rayleigh and Love waves are shown in Figs 7(a) and (b), respectively. 2-D histograms (Figs 7c and d) of the entire phase velocity data set show that most measurements are between 8 and 20 s period. The variability of the phase velocities indicates strong variability of the crustal structure across the area. The gradual decrease of the total number of Rayleigh and Love wave phase velocities at the shortest periods owes to the strong lateral heterogeneities and crustal complexities that affect the measurements. At periods longer than 30 s, the number of Love wave measurements decreases dramatically compared to those for Rayleigh waves. This can be related to the interference of higher modes with the fundamental mode or to the contamination of the transverse component traces with Rayleigh wave energy.

Period-dependent standard deviation of the phase velocities are calculated from the difference between phase velocities from the causal and the acausal parts of the CCFs. Overall, we obtain standard deviations of ~2.5 per cent for Rayleigh waves and ~3.5 per cent for Love waves. They can be related to structural heterogeneity across the study area. The standard deviation values generally decrease with increasing inter-station distances for both Rayleigh and Love wave measurements.

Our approach yields measurements at longer periods than the zero-crossing method (Fig. 8). Especially for small inter-station distances, the relative difference of the maximum period is larger than 8 per cent. If we apply the length criterion (see Section 3.3) to dispersion curves measured with the zero-crossing method, which are shorter in bandwidth, ~10 per cent (Rayleigh) and ~13 per cent (Love) phase velocity dispersion curves would be rejected (red crosses). This affects mostly short paths (<150 km) with maximum periods of 10–20 s and, for that

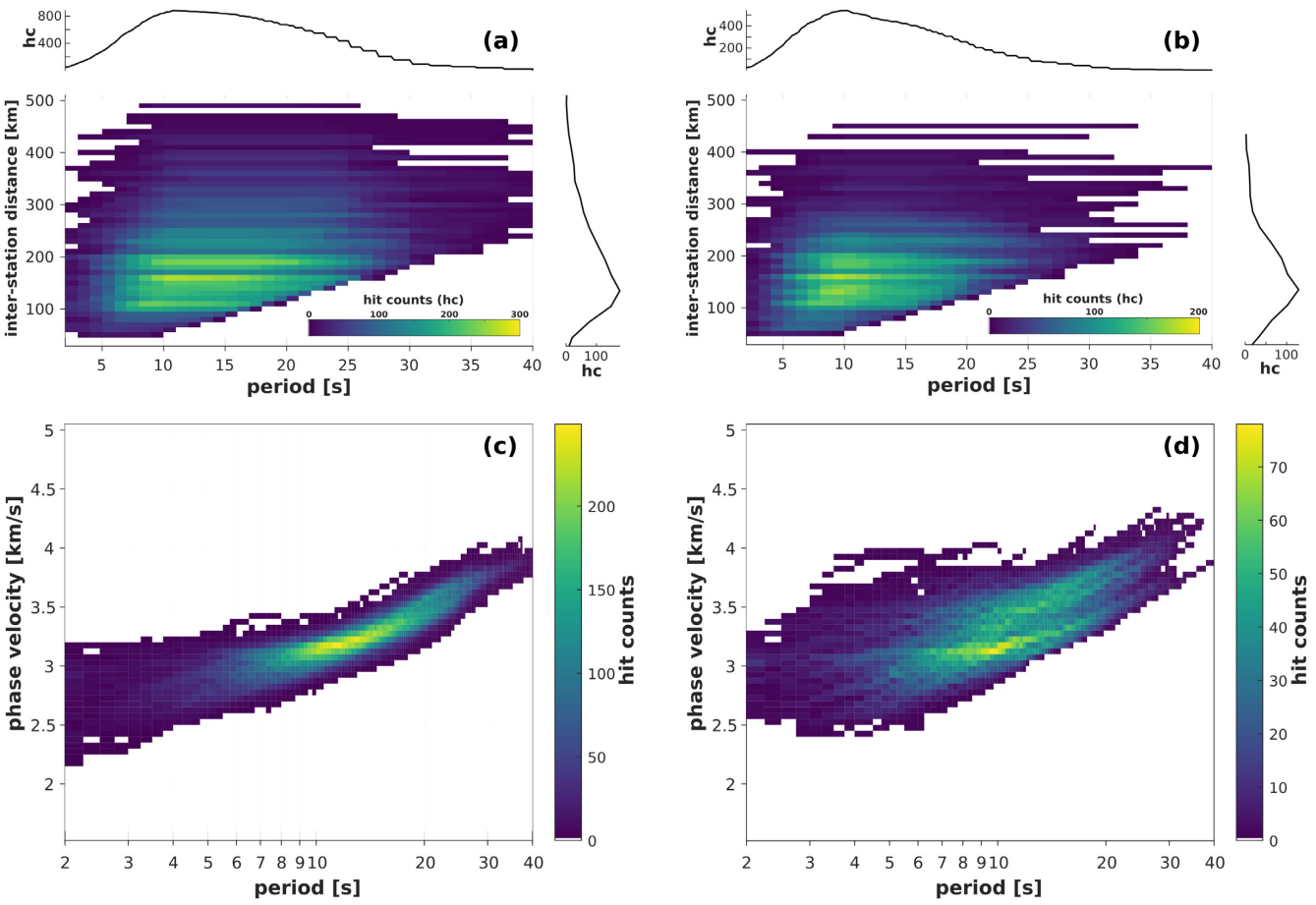

Figure 7. Phase velocity dispersion measurements of the Oman data set. The 2-D histograms show the number of paths as a function of period and inter-station distance for (a) Rayleigh and (b) Love waves. Their corresponding 1-D histograms as function of either period (top) or inter-station distance (right) are also presented. (c,d) Phase velocity dispersion curves are plotted as 2-D histograms in the period range of 2–40 s, respectively.

reason, results in a reduced lateral resolution for Rayleigh wave measurements in the lower crust. On the other hand, Love wave measurements that would not be accepted by the length criterion affect short and long inter-station paths alike. This is due to the overall lower maximum measurable period of Love wave dispersion curves as compared to Rayleigh waves (Fig. 8b) and the consequently shorter dispersion band segments, particularly at larger inter-station distances. In all cases, the maximum obtained periods for both methods are larger than the 3λ criterion for inter-station distances smaller than 250 km (Rayleigh) and 120 km (Love) which illustrates that 3λ is a rather conservative estimate of usable dispersion bandwidth in regional seismic networks.

The automatically measured phase velocities are inverted for 2-D isotropic and azimuthally anisotropic Rayleigh and Love wave phase velocity maps at a set of periods in the range from 3 to 30 s (e.g. Deschamps *et al.* 2008; Fry *et al.* 2010; Endrun *et al.* 2011). The tomographic inversion, which is based on the ray theoretical approximation, is performed using the LSQR (Paige & Saunders 1982) with gradient smoothing and (slight) norm damping as described by Deschamps *et al.* (2008) and Darbyshire & Lebedev (2009). The triangular model grid has a knot spacing of 10 km. Parameters of the inversion at every knot include the isotropic average phase velocity anomaly and additional parameters for anisotropy: 2 parameters for the 4ψ anisotropy for Love waves and 4 parameters for both the 2ψ and 4ψ anisotropy for Rayleigh waves (Smith & Dahlen 1973). About 20 per cent of the phase velocity measurements were discarded due to their high misfit in the *a posteriori* outlier analysis (Lebedev & Van Der Hilst 2008). The resulting phase velocity maps and their resolution are discussed in the following subsections.

4.1 Isotropic Rayleigh and Love phase velocity maps

Isotropic 2-D phase velocity maps for Rayleigh and Love waves at 3, 7 and 12 s are depicted in Fig. 9. Additional isotropic Rayleigh and Love phase velocity maps are shown in Figs S3–S5 in the Supporting Information. To estimate the spatial resolution of the phase velocity maps, we perform checkerboard resolution tests. The checkerboard consists of blocks of alternating positive and negative isotropic velocity anomalies ($\pm$ 500 m s^{-1}), containing no anisotropy, although the inversion allows for it. These anomalies are discretized on block sizes of 30 and 50 km (Fig. 10 for Rayleigh waves and Fig. S2, Supporting Information, for Love waves).

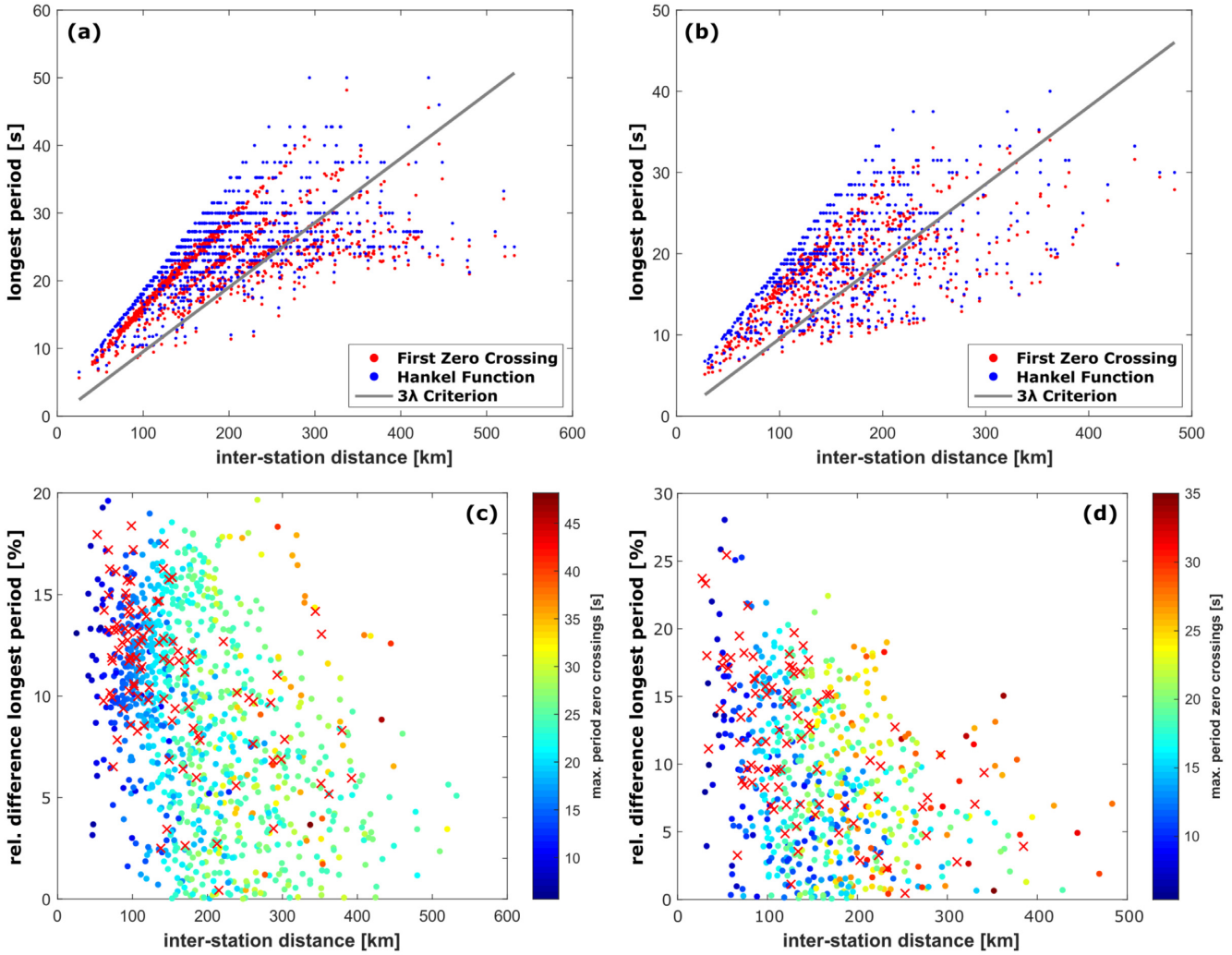

Figure 8. Comparison of the maximum obtained period of (a) Rayleigh and (b) Love wave phase velocity curves in the COOL data set as a function of inter-station distance using the phase of the Hankel Function and the zero-crossing method. Absolute values are compared to the 3λ criterion (grey line). (c, d) The corresponding relative differences of the maximum periods are colour-coded by the maximum period of the zero crossings. Red crosses indicate the paths which would be rejected by the length criterion (see Section 3.3) for the zero-crossing method.

The reconstructed models at periods of 7 and 12 s show that the anomalies are overall well recovered, both in geometry and amplitude, although with a variable lateral resolution due to the uneven ray path coverage. The tests indicate a lateral resolution of about 30 km in the central and eastern part of the study area, whereas it is about 50 km further northwest for both Rayleigh and Love waves.

The depth sensitivity of the phase velocity maps is period dependent (Lebedev *et al.* 2013). At shortest periods (3–7 s), where Rayleigh and Love waves are mostly sensitive to the upper crust, pronounced low phase velocity anomalies are observed in the southwestern foreland of the mountain range. A remarkable change in the phase velocities towards higher values is observed along the mountain range. This transition is subparallel to the obduction frontal thrust and the high velocities across the Al-Hajar mountains reflect the presence of the Semail ophiolite nappes and the autochtonous shelf sediments and basement of the Al-Hajar mountains. High velocities are also observed in the Jebel Akhdar and Saih Hatat domes as well as in the Hawasina window. The easternmost part of the study area also shows high phase velocities, which can be related to mafic intrusions from mid-Ordovician to Permian times that are exposed in the Huqf high further south. Our data suggest that this shallow basement may be extending further north (Oterdoom *et al.* 1999). At the same periods, Love wave phase velocity heterogeneity is generally comparable to the Rayleigh wave phase velocities. The differences between the two relate to differences of the depth sensitivity of the waves and to radial anisotropy, which we will discuss in detail in a separate publication (Weidle *et al.* 2022).

The phase velocity map at 12 s period is sensitive to middle and lower crustal structure and indicates high velocity anomalies in the central part of the mountain range, especially at the Saih Hatat dome and further east. This suggests that the middle to lower crust in the east is structurally different from the one in the northwest of the study area. The Love phase velocity map at 12 s shows a very similar pattern but indicates a more pronounced positive anomaly across the Jebel Akhdar Dome and Hawasina window. In contrast, negative anomalies are imaged to the south and southwest in both Rayleigh and Love wave maps. At longer periods (Figs S4 and S5, Supporting Information), a gradual increase in the phase velocities is observed from the northwest to the southeast, suggesting a distinct change in lower crustal

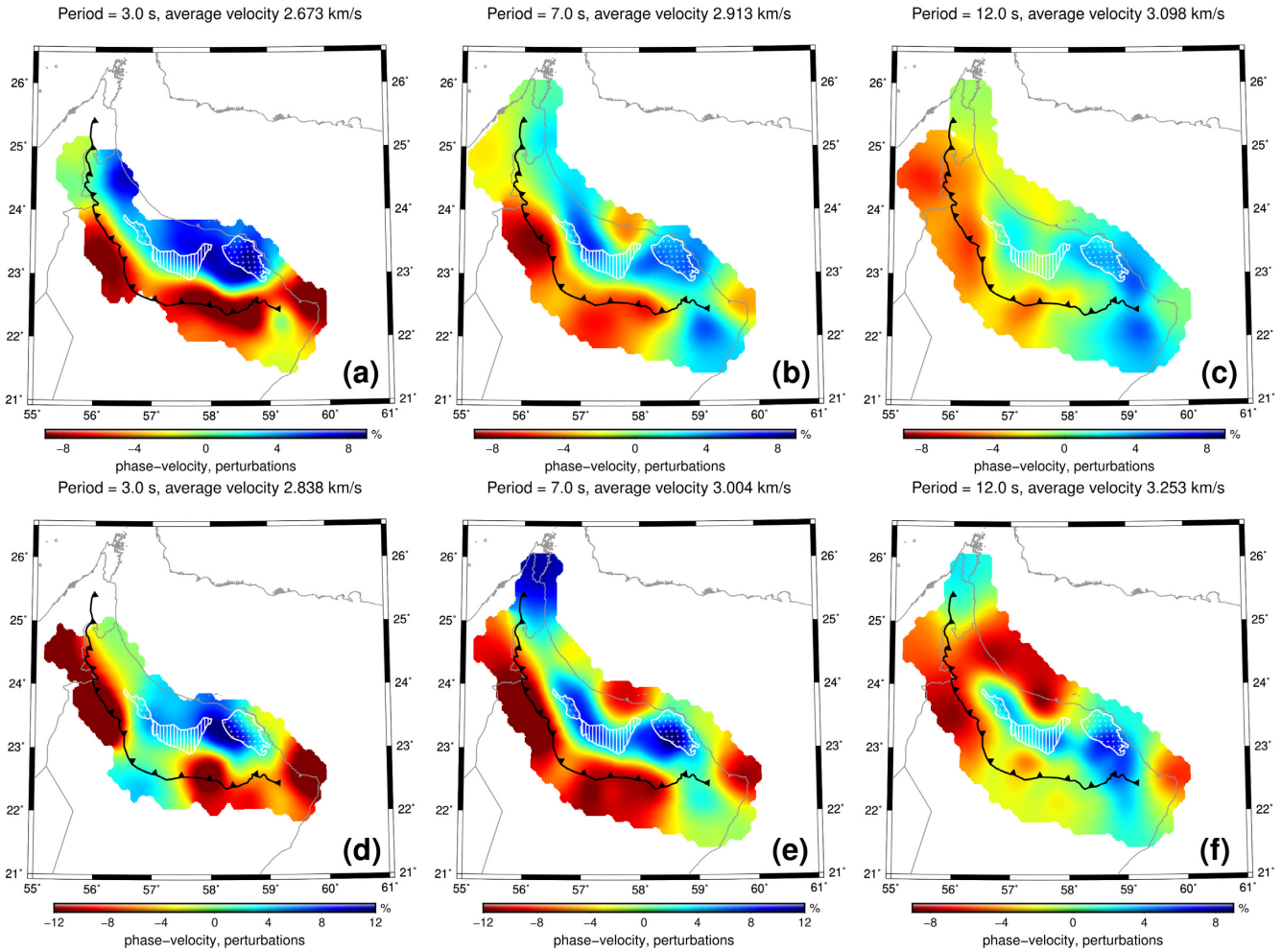

Figure 9. Isotropic (a)–(c) Rayleigh and (d)–(f) Love wave phase velocity maps at periods of 3, 7 and 12 s. Phase velocity perturbations are plotted relative to the regional average phase velocity value at the corresponding period, given at the top of each map. White hatched polygons indicate the tectonic features as modified after Fig. 1.

properties. This change also agrees with an eastward shallowing Moho, suggested by gravity measurements (Jiménez-Munt *et al.* 2012; Mechie *et al.* 2013).

4.2 Azimuthally anisotropic Rayleigh wave phase velocity maps

Examples of the period-dependent azimuthally anisotropic maps of Rayleigh wave phase velocities at 3, 7 and 12 s periods are shown in Figs 11 and 12. The Rayleigh wave fast propagation direction are shown as bars on the different maps. To investigate their reliability, we apply a 90° rotation test, in which the 2ψ anisotropy terms are rotated by 90° and the 4ψ anisotropy are set to zero (e.g. Zhang *et al.* 2009; Endrun *et al.* 2011; Schaeffer *et al.* 2016). Fig. 11 illustrates the rotation test at a period of 3 s. From the anisotropic path coverage map (Fig. 11b) we can expect good isotropic (see Fig. 10) as well as anisotropic resolution in the central and eastern part of the study area. After inverting the constructed synthetic model we compare the fast directions of the 2ψ anisotropy and the amplitudes of the rotated models before and after the inversion (Fig. 11c). We apply two criteria to automatically identify the well-resolved anisotropy nodes based on (1) the difference in fast direction and (2) deviation in the anisotropy amplitude (Fig. 11d). A node is considered resolved if the difference in fast direction between the rotated models is less than 40° and the amplitude deviation is less than 50 per cent. Significant differences in directions and amplitudes between the models would indicate that the original anisotropic phase velocity maps have artificial anisotropic anomalies due to the limited path coverage and the leakage of isotropic heterogeneity into anisotropy (e.g. Darbyshire & Lebedev 2009).

Our tests indicate good recovery of the amplitude and the fast directions of anisotropy in areas of good path coverage. At 3 s period, the fast directions are parallel to the strike of the mountain range. The best resolution is obtained east of the Semail Gap Fault, a major fault at the eastern margin of the Jebel Akhdar Dome (e.g. Scharf *et al.* 2019), across the Saih Hatat Dome and further south, showing mostly an E-W to SE-SW fast direction with 4–6 per cent of 2ψ-anisotropy. Further south of the mountain range, especially in the foreland basins, a gradual decrease in the amplitudes of the anisotropy is observed. Arc-parallel anisotropy is often observed in the shallow crust of the mountain belts

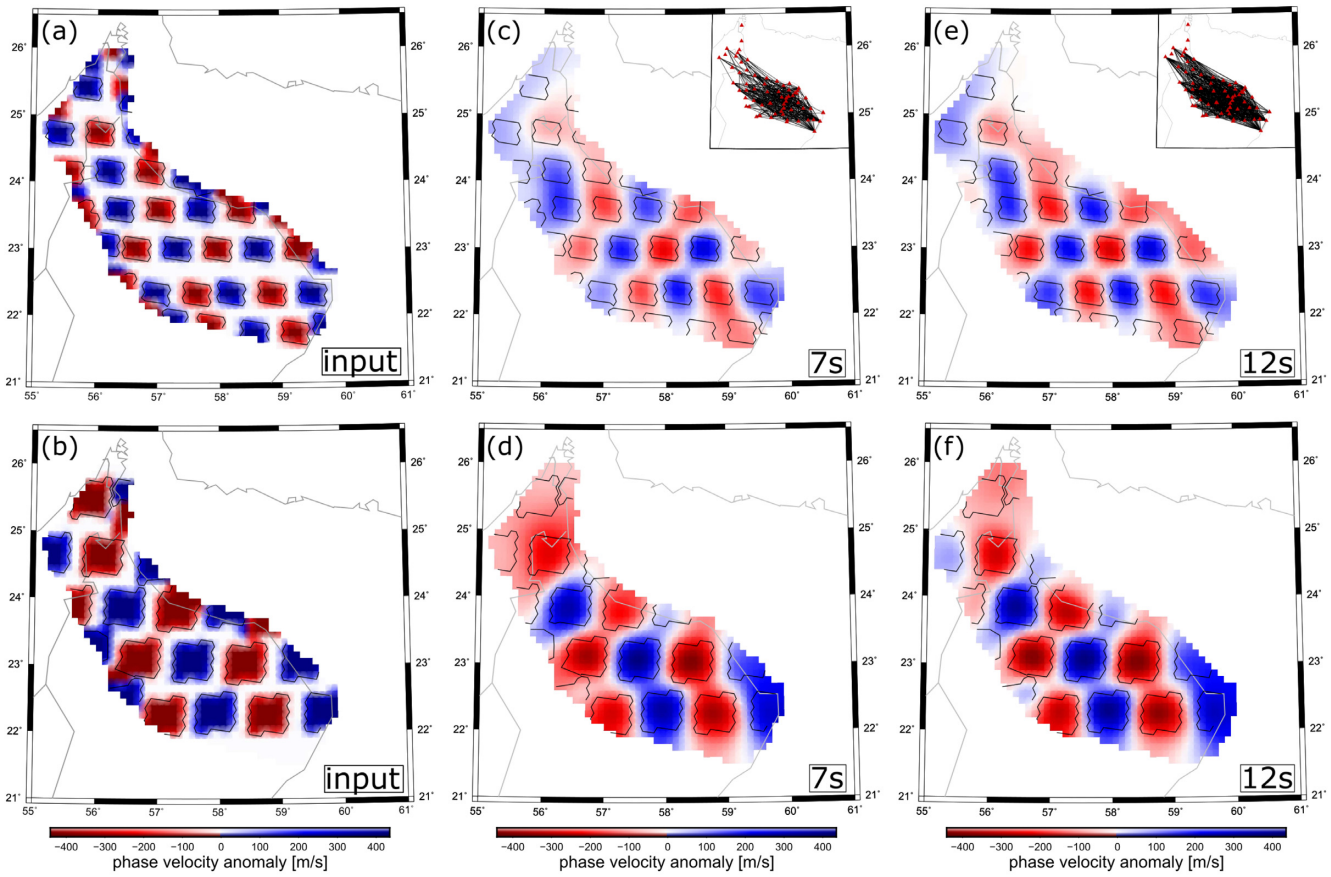

Figure 10. Isotropic checkerboard tests for Rayleigh waves with anomalies of (a, c, e) 30 km and (b, d, f) 50 km size. Solid contour lines mark input anomalies.

and interpreted as structural anisotropy due to deformation. In northern Oman, the direction coincides with the strike of the allochtonous units (NW-SE).

The anisotropic phase velocity map at 7 s period indicates the dominance of two different fast directions across the mountain range. While the strong NE-SW fast directions persist to the east of the Semail Gap, NW-SE fast directions in combination with an pronounced positive velocity anomaly are dominant to the west of the Semail Gap in the area of the Hawasina window. This change in the fast orientation azimuth is consistent with a segmentation of the Arabian continental margin prior and during obduction, as interpreted from sedimentary records offshore (Ninkabou *et al.* 2021).

At 12 s period, fast propagation orientations are overall N-S across the mountain range, whereas they are mostly NW-SE in the foreland basins area in the south. These fast propagation directions are distinctly different from those at shorter periods and may be attributed to frozen-in extensional deformation in the lower crust (Mainprice & Nicolas 1989).

5 CONCLUSIONS

We presented and discussed a new automated processing scheme to exploit the phase of ambient noise cross correlations in the determination of Rayleigh and Love wave phase velocities. After applying a frequency-dependent filtering and weighting scheme, we match the phase of the CCF spectrum to the phase of the Hankel function to obtain dispersion curve measurements as continuous function of frequency over a broad period range (2–40 s). Synthetic as well as real tests show that robust measurements can be obtained even in the presence of noisy spectra, however, spectral smoothing is in practice needed to obtain smooth dispersion curves. Using the phase extends the bandwidths of dispersion measurements to longer periods, in particular for short inter-station distances. For Rayleigh as well as for Love wave measurements, our tests indicate that the 3λ criterion of Bensen *et al.* (2007) is a conservative measure and can be relaxed in typical applications.

The application of the presented method to the COOL data set in northern Oman yields phase velocity measurements (1072 Rayleigh and 663 Love wave curves) in a broad period range (2–40 s) with small standard deviations. Period-dependent 2-D isotropic and azimuthally anisotropic Rayleigh and Love wave phase velocity maps are constructed by means of tomographic inversions. The maps reflect striking features of the continental middle to lower crust below the Semail ophiolite and suggest different crustal architectures between the northern and eastern Oman Mountains. Azimuthal anisotropy indicates segmentation of the margin across the Semail Gap Fault Zone and shows contrasting fast directions in the shallow and deep crust.

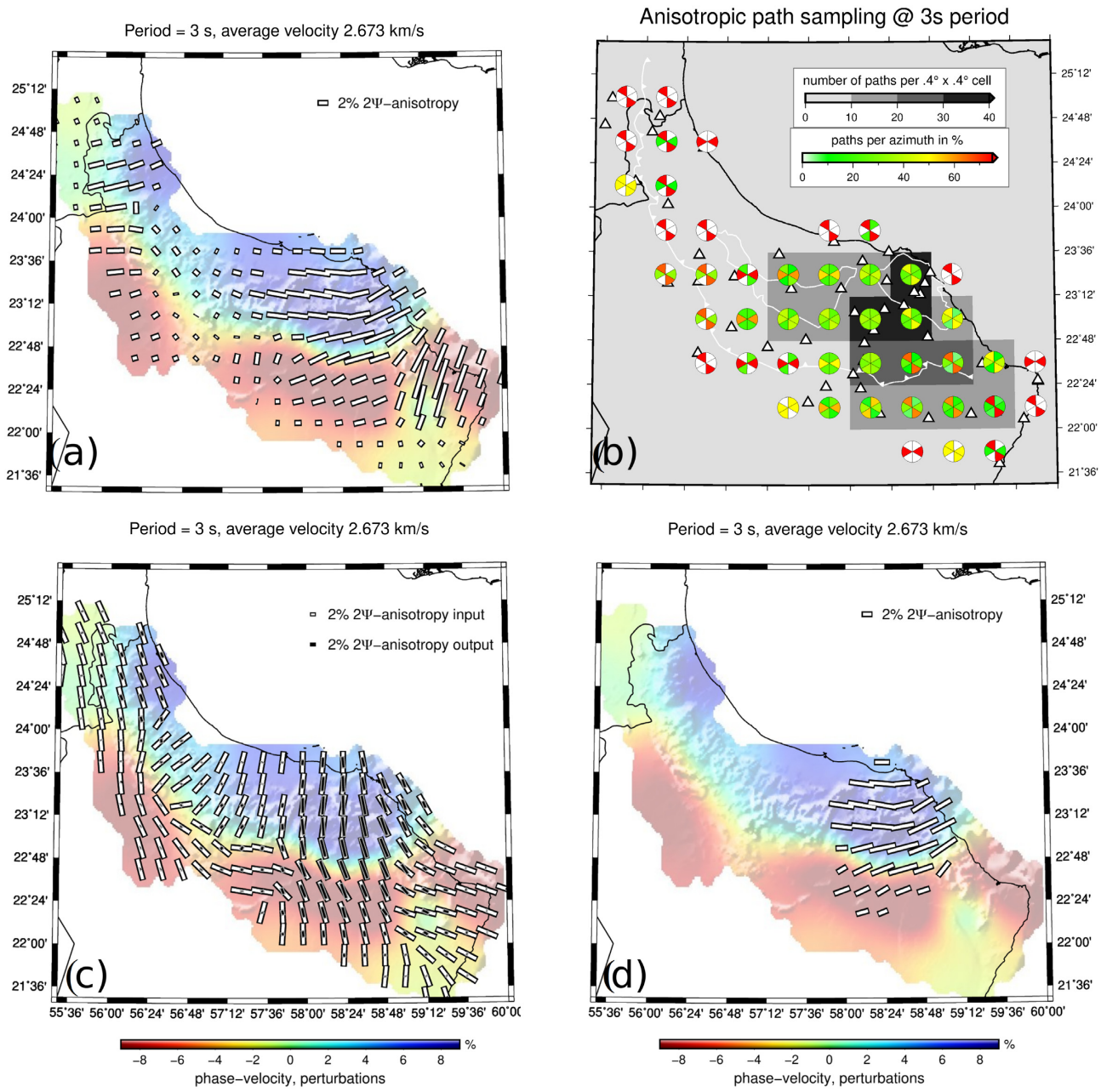

Figure 11. Results of anisotropy reliability test. (a) Original Rayleigh wave phase velocity map at a period of 3 s. The length and the direction of the bars denote the amplitude and the fast-propagation direction of the 2ψ anisotropy, respectively. (b) Ray path density coverage at the same period. While the number of paths per each $0.4^\circ \times 0.4^\circ$ cell is shown in grey colour scale, the number of paths per azimuth (in percent) is colour-coded. White triangles indicate the seismic stations included in the analysis. (c) The input model for the rotation test where the 2ψ anisotropy directions are rotated by 90° (white bars). The rotated 2ψ anisotropy bars resulted from the inversion are shown as black bars. (d) Well-resolved azimuthally anisotropic phase velocity map at 3 s.

ACKNOWLEDGMENTS

We thank Victor Tsai and an anonymous reviewer and the Editor, Huajian Yao, for constructive comments and suggestions that helped us to improve the manuscript. The COOL temporary seismic experiment was a collaborative initiative by Prof Philippe Agard (Université Pierre et Marie Curie, Paris, France) and Dr Christian Weidle and Prof Thomas Meier (Christian-Albrechts-University Kiel). We wish to thank Céline Ducassou and the German University of Technology (GUtech), Oman, Dr Issa El-Hussain and staff from Earthquake Monitoring Center at Sultan Qaboos University (SQU), Oman and Cécile Prigent (UJF Grenoble, now at IPG Paris, France) for their enormous support during the period of the seismic experiment and for sharing waveform data from the Oman Seismic Network. Numerous GUtech and SQU students are thanked for their participation in the field work. Seismic equipment for the deployment was provided by the German Geophysical Instrument Pool (GIPP) at GeoForschungsZentrum Potsdam. We thank Dr Kamal Atiya from the Dubai Seismic Network for facilitating data usage, and acknowledge use of data from IRIS/IDA Global Seismic Network station II.UOSS (Scripps Institution Of Oceanography 1986). LW and

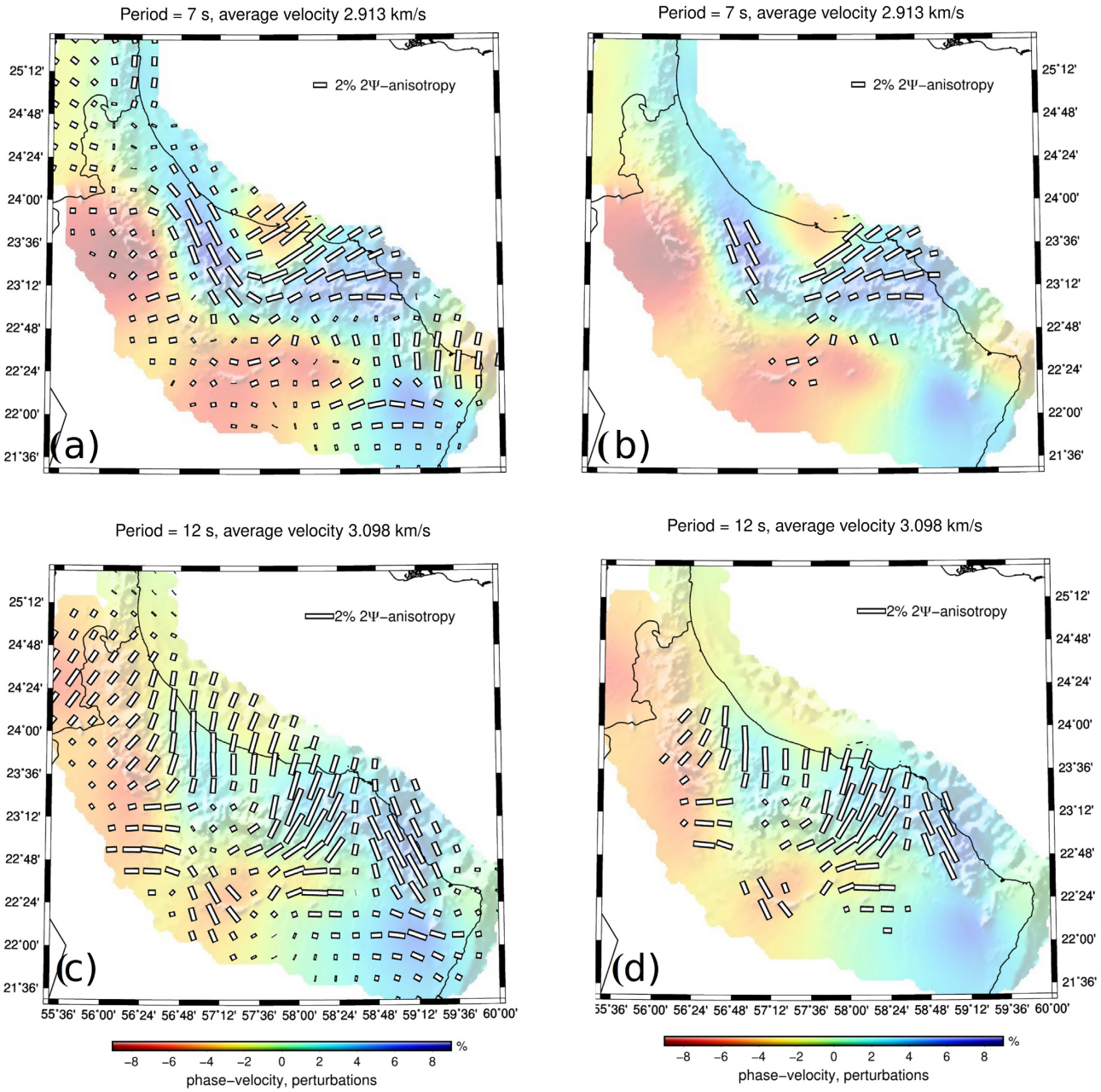

Figure 12. Azimuthally anisotropic Rayleigh wave phase velocity maps at periods of 7 and 12 s before (left) and after (right) applying the 90° rotation test. The length and the direction of the bars denote the amplitude and the fast-propagation direction of anisotropy, respectively.

AE were supported by DFG project WE 4069/6-1. AE acknowledges funding from the German Science Foundation (SPP-2017: grant ME 1320/8-1).

DATA AVAILABILITY

Seismic waveform data from the temporary experiment (https://doi.org/10.7914/SN/5H_2013) can be obtained from the GEOFON data centre of the GFZ German Research Centre for Geosciences (https://geofon.gfz-potsdam.de/). Data from Oman and Dubai Seismic Network stations in the project period can be obtained from the authors upon request. Data from Global Seismic Network Stations used in this study (https://doi.org/10.7914/SN/II) are distributed by IRIS Data Management Center (https://ds.iris.edu/).

REFERENCES

Abramowitz, M. & Stegun, I., 1964. *Handbook of Mathematical Functions: with Formulas, Graphs, and Mathematical Tables,* Dover Books on Mathematics, Dover Publications.

Aki, K., 1957. Space and time spectra of stationary stochastic waves, with special reference to microtremors, *Bull. Earthq. Res. Inst.,* **35,** 415–456.

Aki, K. & Richards, P.G., 2002. *Quantitative Seismology,* University Science Books Sausalito California.

Bensen, G., Ritzwoller, M., Barmin, M., Levshin, A.L., Lin, F., Moschetti, M., Shapiro, N. & Yang, Y., 2007. Processing seismic ambient noise data to obtain reliable broad-band surface wave dispersion measurements, *Geophys. J. Int.,* **169**(3), 1239–1260.

Bensen, G., Ritzwoller, M. & Shapiro, N.M., 2008. Broadband ambient noise surface wave tomography across the united states, *J. geophys. Res.: Solid Earth,* **113**(B5), doi:10.1029/2007JB005248.

Bonadio, R. *et al.*, 2021. Optimal resolution tomography with error tracking and the structure of the crust and upper mantle beneath Ireland and Britain, *Geophys. J. Int.,* **226**(3), 2158–2188.

Boschi, L. & Weemstra, C., 2015. Stationary-phase integrals in the cross correlation of ambient noise, *Rev. Geophys.,* **53**(2), 411–451.

Boschi, L., Weemstra, C., Verbeke, J., Ekström, G., Zunino, A. & Giardini, D., 2012. On measuring surface wave phase velocity from station–station cross-correlation of ambient signal, *Geophys. J. Int.,* **192**(1), 346–358.

Claerbout, J.F., 1968. Synthesis of a layered medium from its acoustic transmission response, *Geophysics,* **33**(2), 264–269.

Cupillard, P. & Capdeville, Y., 2010. On the amplitude of surface waves obtained by noise correlation and the capability to recover the attenuation: a numerical approach, *Geophys. J. Int.,* **181**(3), 1687–1700.

Darbyshire, F.A. & Lebedev, S., 2009. Rayleigh wave phase-velocity heterogeneity and multilayered azimuthal anisotropy of the Superior Craton, Ontario, *Geophys. J. Int.,* **176**(1), 215–234.

Derode, A., Larose, E., Campillo, M. & Fink, M., 2003. How to estimate the green's function of a heterogeneous medium between two passive sensors? Application to acoustic waves, *Appl. Phys. Lett.,* **83**(15), 3054–3056.

Deschamps, F., Lebedev, S., Meier, T. & Trampert, J., 2008. Azimuthal anisotropy of Rayleigh-wave phase velocities in the east-central United States, *Geophys. J. Int.,* **173**(3), 827–843.

Dziewonski, A.M. & Anderson, D.L., 1981. Preliminary reference earth model, *Phys. Earth planet. Inter.,* **25**(4), 297–356.

Dziewonski, A., Bloch, S. & Landisman, M., 1969. A technique for the analysis of transient seismic signals, *Bull. seism. Soc. Am.,* **59**(1), 427–444.

Ekström, G., 2017. Short-period surface-wave phase velocities across the conterminous United States, *Phys. Earth planet. Inter.,* **270,** 168–175.

Ekström, G., Abers, G.A. & Webb, S.C., 2009. Determination of surface-wave phase velocities across USArray from noise and Aki's spectral formulation, *Geophys. Res. Lett.,* **36**(18), doi:10.1029/2009GL039131.

El-Sharkawy, A., Meier, T., Lebedev, S., Behrmann, J.H., Hamada, M., Cristiano, L., Weidle, C. & Köhn, D., 2020. The slab puzzle of the alpine-mediterranean region: Insights from a new, high-resolution, shear wave velocity model of the upper mantle, *Geochem. Geophys. Geosyst.,* **21**(8), e2020GC008993, doi:10.1029/2020GC008993.

Endrun, B., Meier, T., Bischoff, M. & Harjes, H.-P., 2004. Lithospheric structure in the area of crete constrained by receiver functions and dispersion analysis of rayleigh phase velocities, *Geophys. J. Int.,* **158**(2), 592–608.

Endrun, B., Lebedev, S., Meier, T., Tirel, C. & Friederich, W., 2011. Complex layered deformation within the aegean crust and mantle revealed by seismic anisotropy, *Nat. Geosci.,* **4**(3), 203–207.

Ermert, L., Villasenor, A. & Fichtner, A., 2016. Cross-correlation imaging of ambient noise sources, *Geophys. J. Int.,* **204**(1), 347–364.

Fichtner, A., 2014. Source and processing effects on noise correlations, *Geophys. J. Int.,* **197**(3), 1527–1531.

Fichtner, A., 2015. Source-structure trade-offs in ambient noise correlations, *Geophys. J. Int.,* **202**(1), 678–694.

Fichtner, A. & Tsai, V., 2019. Theoretical foundations of noise interferometry, in *Seismic Ambient Noise,* eds, Nakata, N., Gualtieri, L. & Fichtner, A., pp. 109–143,Cambridge University Press.

Froment, B., Campillo, M., Roux, P., Gouédard, P., Verdel, A. & Weaver, R.L., 2010. Estimation of the effect of nonisotropically distributed energy on the apparent arrival time in correlations, *Geophysics,* **75**(5), SA85–SA93.

Fry, B., Deschamps, F., Kissling, E., Stehly, L. & Giardini, D., 2010. Layered azimuthal anisotropy of rayleigh wave phase velocities in the european alpine lithosphere inferred from ambient noise, *Earth planet. Sci. Lett.,* **297**(1–2), 95–102.

Gouedard, P. *et al.*, 2008. Cross-correlation of random fields: mathematical approach and applications, *Geophys. Prospect.,* **56**(3), 375–393.

Gudmundsson, O., Khan, A. & Voss, P., 2007. Rayleigh-wave group-velocity of the icelandic crust from correlation of ambient seismic noise, *Geophys. Res. Lett.,* **34**(14), doi:10.1029/2007GL030215.

Halliday, D. & Curtis, A., 2008. Seismic interferometry, surface waves and source distribution, *Geophys. J. Int.,* **175**(3), 1067–1087.

Haney, M.M., Mikesell, T.D., van Wijk, K. & Nakahara, H., 2012. Extension of the spatial autocorrelation (SPAC) method to mixed-component correlations of surface waves, *Geophys. J. Int.,* **191**(1), 189–206.

Hillers, G., Graham, N., Campillo, M., Kedar, S., Landès, M. & Shapiro, N., 2012. Global oceanic microseism sources as seen by seismic arrays and predicted by wave action models, *Geochem. Geophys. Geosyst.,* **13**(1), doi:10.1029/2011GC003875.

Jiménez-Munt, I., Fernàndez, M., Saura, E., Vergés, J. & Garcia-Castellanos, D., 2012. 3-d lithospheric structure and regional/residual bouguer anomalies in the Arabia—Eurasia collision (iran), *Geophys. J. Int.,* **190**(3), 1311–1324.

Juretzek, C. & Hadziioannou, C., 2016. Where do ocean microseisms come from? a study of Love-to-Rayleigh wave ratios, *J. geophys. Res.: Solid Earth,* **121**(9), 6741–6756.

Kästle, E.D., Soomro, R., Weemstra, C., Boschi, L. & Meier, T., 2016. Two-receiver measurements of phase velocity: cross-validation of ambient-noise and earthquake-based observations, *Geophys. J. Int.,* **207**(3), 1493–1512.

Kästle, E.D., El-Sharkawy, A., Boschi, L., Meier, T., Rosenberg, C., Bellahsen, N., Cristiano, L. & Weidle, C., 2018. Surface wave tomography of the alps using ambient-noise and earthquake phase velocity measurements, *J. geophys. Res.: Solid Earth,* **123**(2), 1770–1792.

Larose, E., Derode, A., Clorennec, D., Margerin, L. & Campillo, M., 2005. Passive retrieval of Rayleigh waves in disordered elastic media, *Phys. Rev. E,* **72**(4), 046607, doi:10.1103/PhysRevE.72.046607.

Laske, G., Masters, G., Ma, Z. & Pasyanos, M., 2013. Update on CRUST1.0—a 1-degree global model of Earth's crust, in *Geophys. Res. Abstr,* Vol. **15,** p. 2658, EGU General Assembly Vienna, Austria.

Lebedev, S. & Van Der Hilst, R.D., 2008. Global upper-mantle tomography with the automated multimode inversion of surface and S-wave forms, *Geophys. J. Int.,* **173**(2), 505–518.

Lebedev, S., Adam, J. M.-C. & Meier, T., 2013. Mapping the moho with seismic surface waves: a review, resolution analysis, and recommended inversion strategies, *Tectonophysics,* **609,** 377–394.

Levshin, A., Yanovskaya, T., Its, E., Lander, A., Bukchin, B., Barmin, M. & Ratnikova, L., 2012.*Seismic Surface Waves in a Laterally Inhomogeneous Earth,* Vol. **9,** pp. 153–163, Keilis-Borok, V.I., Springer Science & Business Media.

Li, H., Bernardi, F. & Michelini, A., 2010. Love wave tomography in Italy from seismic ambient noise, *Earthq. Sci.,* **23**(5), 487–495.

Lin, F.-C., Moschetti, M.P. & Ritzwoller, M.H., 2008. Surface wave tomography of the western united states from ambient seismic noise: Rayleigh and love wave phase velocity maps, *Geophys. J. Int.,* **173**(1), 281–298.

Lin, F.-C., Li, D., Clayton, R.W. & Hollis, D., 2013. High-resolution 3d shallow crustal structure in long beach, California: application of ambient noise tomography on a dense seismic array, *Geophysics,* **78**(4), Q45–Q56.

Lobkis, O.I. & Weaver, R.L., 2001. On the emergence of the green's function in the correlations of a diffuse field, *J. acoust. Soc. Am.,* **110**(6), 3011–3017.

Luo, Y., Yang, Y., Xu, Y., Xu, H., Zhao, K. & Wang, K., 2015. On the limitations of interstation distances in ambient noise tomography, *Geophys. J. Int.,* **201**(2), 652–661.

Mainprice, D. & Nicolas, A., 1989. Development of shape and lattice preferred orientations: application to the seismic anisotropy of the lower crust, *J. Struct. Geol.,* **11**(1–2), 175–189.

Mechie, J., Ben-Avraham, Z., Weber, M.H., Götze, H.-J., Koulakov, I., Mohsen, A. & Stiller, M., 2013. The distribution of Moho depths beneath the arabian plate and margins, *Tectonophysics,* **609,** 234–249.

Meier, T., Dietrich, K., Stöckhert, B. & Harjes, H.-P., 2004. One-dimensional models of shear wave velocity for the eastern Mediterranean obtained from the inversion of Rayleigh wave phase velocities and tectonic implications, *Geophys. J. Int.,* **156**(1), 45–58.

Menke, W. & Jin, G., 2015. Waveform fitting of cross spectra to determine phase velocity using aki's formula, *Bull. seism. Soc. Am.,* **105**(3), 1619–1627.

Molinari, I., Verbeke, J., Boschi, L., Kissling, E. & Morelli, A., 2015. Italian and a Lpine three-dimensional crustal structure imaged by ambient-noise surface-wave dispersion, *Geochem. Geophys. Geosyst.,* **16**(12), 4405–4421.

Nakahara, H., 2006. A systematic study of theoretical relations between spatial correlation and green's function in one-, two-and three-dimensional random scalar wavefields, *Geophys. J. Int.,* **167**(3), 1097–1105.

Nicolas, A. & Boudier, F., 2011. Structure and dynamics of ridge axial melt lenses in the oman ophiolite, *J. geophys. Res.: Solid Earth,* **116**(B3), doi:10.1029/2010JB007934.

Ninkabou, D. *et al.*, 2021. Structure of the offshore obducted oman margin: emplacement of semail ophiolite and role of tectonic inheritance, *J. geophys. Res.: Solid Earth,* **126**(2), 2020JB020187, doi:10.1029/2020JB020187.

Oterdoom, W.H., Worthing, M.A. & Partington, M., 1999. Petrological and tectonostratigraphic evidence for a mid ordovician rift pulse on the arabian peninsula, *GeoArabia,* **4**(4), 467–500.

Paige, C.C. & Saunders, M.A., 1982. Lsqr: An algorithm for sparse linear equations and sparse least squares, *ACM Trans. Math. Softw.,* **8**(1), 43–71.

Paul, A., Campillo, M., Margerin, L., Larose, E. & Derode, A., 2005. Empirical synthesis of time-asymmetrical green functions from the correlation of coda waves, *J. geophys. Res.: Solid Earth,* **110**(B8), doi:10.1029/2004JB003521.

Picozzi, M., Parolai, S., Bindi, D. & Strollo, A., 2009. Characterization of shallow geology by high-frequency seismic noise tomography, *Geophys. J. Int.,* **176**(1), 164–174.

Ritzwoller, M.H. & Levshin, A.L., 1998. Eurasian surface wave tomography: group velocities, *J. geophys. Res.: Solid Earth,* **103**(B3), 4839–4878.

Roux, P., Sabra, K.G., Kuperman, W.A. & Roux, A., 2005. Ambient noise cross correlation in free space: theoretical approach, *J. acoust. Soc. Am.,* **117**(1), 79–84.

Ryberg, T., Muksin, U. & Bauer, K., 2016. Ambient seismic noise tomography reveals a hidden caldera and its relation to the tarutung pull-apart basin at the sumatran fault zone, indonesia, *J. Volc. Geotherm. Res.,* **321,** 73–84.

Sabra, K.G., Gerstoft, P., Roux, P., Kuperman, W. & Fehler, M.C., 2005. Extracting time-domain green's function estimates from ambient seismic noise, *Geophys. Res. Lett.,* **32**(3), doi:10.1029/2004GL021862.

Sánchez-Sesma, F.J. & Campillo, M., 2006. Retrieval of the Green's function from cross correlation: the canonical elastic problem, *Bull. seism. Soc. Am.,* **96**(3), 1182–1191.

Schaeffer, A., Lebedev, S. & Becker, T., 2016. Azimuthal seismic anisotropy in the earth's upper mantle and the thickness of tectonic plates, *Geophys. Suppl. Mon. Not. R. Astron. Soc.,* **207**(2), 901–933.

Scharf, A., Mattern, F., Moraetis, D., Callegari, I. & Weidle, C., 2019. Postobductional kinematic evolution and geomorphology of a major regional structure—the semail gap fault zone (oman mountains), *Tectonics,* **38**(8), 2756–2778.

Shapiro, N.M. & Campillo, M., 2004. Emergence of broadband Rayleigh waves from correlations of the ambient seismic noise, *Geophys. Res. Lett.,* **31**(7), doi:10.1029/2004GL019491.

Shapiro, N.M., Campillo, M., Stehly, L. & Ritzwoller, M.H., 2005. High-resolution surface-wave tomography from ambient seismic noise, *Science,* **307**(5715), 1615–1618.

Smith, M.L. & Dahlen, F., 1973. The azimuthal dependence of love and rayleigh wave propagation in a slightly anisotropic medium, *J. geophys. Res.,* **78**(17), 3321–3333.

Snieder, R., 2004. Extracting the Green's function from the correlation of coda waves: a derivation based on stationary phase, *Phys. Rev. E,* **69**(4), 046610, doi:10.1103/PhysRevE.69.046610.

Soomro, R., Weidle, C., Cristiano, L., Lebedev, S., Meier, T. & Group, P.W., 2016. Phase velocities of Rayleigh and Love waves in central and northern Europe from automated, broad-band, interstation measurements, *Geophys. J. Int.,* **204**(1), 517–534.

Stehly, L. & Boué, P., 2017. On the interpretation of the amplitude decay of noise correlations computed along a line of receivers, *Geophys. J. Int.,* **209**(1), 358–372.

Stehly, L., Campillo, M. & Shapiro, N., 2006. A study of the seismic noise from its long-range correlation properties, *J. geophys. Res.: Solid Earth,* **111**(B10), doi:10.1029/2005JB004237.

Stork, A.L., Allmark, C., Curtis, A., Kendall, J.-M. & White, D.J., 2018. Assessing the potential to use repeated ambient noise seismic tomography to detect co2 leaks: Application to the aquistore storage site, *Int. J. Greenhouse Gas Contr.,* **71,** 20–35.

Tsai, V.C., 2009. On establishing the accuracy of noise tomography traveltime measurements in a realistic medium, *Geophys. J. Int.,* **178**(3), 1555–1564.

Tsai, V.C. & Moschetti, M.P., 2010. An explicit relationship between time-domain noise correlation and spatial autocorrelation (spac) results, *Geophys. J. Int.,* **182**(1), 454–460.

Verbeke, J., Boschi, L., Stehly, L., Kissling, E. & Michelini, A., 2012. High-resolution rayleigh-wave velocity maps of central europe from a dense ambient-noise data set, *Geophys. J. Int.,* **188**(3), 1173–1187.

Wang, Y., Lin, F.-C., Schmandt, B. & Farrell, J., 2017. Ambient noise tomography across mount st. helens using a dense seismic array, *J. geophys. Res.: Solid Earth,* **122**(6), 4492–4508.

Wapenaar, K., 2004. Retrieving the elastodynamic green's function of an arbitrary inhomogeneous medium by cross correlation, *Phys. Rev. Lett.,* **93**(25), 254301, doi:10.1103/PhysRevLett.93.254301.

Weaver, R.L. & Lobkis, O.I., 2001. Ultrasonics without a source: thermal fluctuation correlations at mhz frequencies, *Phys. Rev. Lett.,* **87**(13), 134301, doi:10.1103/PhysRevLett.87.134301.

Weaver, R.L. & Lobkis, O.I., 2004. Diffuse fields in open systems and the emergence of the green's function (l), *J. acoust. Soc. Am.,* **116**(5), 2731–2734.

Weemstra, C., Snieder, R. & Boschi, L., 2015. On the estimation of attenuation from the ambient seismic field: inferences from distributions of isotropic point scatterers, *Geophys. J. Int.,* **203**(2), 1054–1071.

Weidle, C., Agard, P., Meier, T., Ducassou, C. & El-Hussain, I., 2013. Cool (crust of the oman ophiolite and its lithosphere) seismic network, *GEOFON Data Archive* , doi:10.7914/SN/5H_2013.

Weidle, C., Wiesenberg, L., Krüger, F., Scharf, A., Agard, P., El-Sharkawy, A. & Meier, T., 2022. A 3-d crustal shear wave velocity model and moho map below the semail ophiolite, Oman, *Geophys. J. Int.,* doi:10.1093/gji/ggac223.

Yang, Y., Ritzwoller, M.H., Levshin, A.L. & Shapiro, N.M., 2007. Ambient noise Rayleigh wave tomography across Europe, *Geophys. J. Int.,* **168**(1), 259–274.

Yao, H. & Van Der Hilst, R.D., 2009. Analysis of ambient noise energy distribution and phase velocity bias in ambient noise tomography, with application to se tibet, *Geophys. J. Int.,* **179**(2), 1113–1132.

Yao, H., van Der Hilst, R.D. & De Hoop, M.V., 2006. Surface-wave array tomography in SE Tibet from ambient seismic noise and two-station analysis—I. Phase velocity maps, *Geophys. J. Int.,* **166**(2), 732–744.

Zhang, X., Paulssen, H., Lebedev, S. & Meier, T., 2009. 3d shear velocity structure beneath the gulf of California from Rayleigh wave dispersion, *Earth planet. Sci. Lett.,* **279**(3–4), 255–262.

SUPPORTING INFORMATION

Supplementary data are available at *GJI* online.

Figure S1. Effect of applying a taper on the real part of the cross-spectrum. The theoretical solution of the Bessel function, Neumann function, Struve function and the Hilbert transform of the Bessel function (a) untapered and (c) tapered are shown as a function of ω using a constant velocity $c = 4$ km s^{-1} and an inter-station distance of 100 km. The grey dashed line shows the applied taper. The respective (b) untapered and (d) tapered phases are shown on the right side, calculated using eqs (9)–(11).

Figure S2. Isotropic checkerboard tests for Love waves with anomalies of (a, c, e) 30 km and (b, d, f) 50 km size. Solid contour lines mark input anomalies.

Figure S3. Isotropic (top) Rayleigh and (bottom) Love wave phase velocity maps at periods of 5, 8 and 10 s. Phase velocity perturbations are plotted relative to a regional average phase velocity value at the corresponding period given on top of each map. Hatched polygons indicate the tectonic features drawn after Fig. 1.

Figure S4. Isotropic (top) Rayleigh and (bottom) Love wave phase velocity maps at periods of 15, 18 and 20 s. Phase velocity perturbations are plotted relative to a regional average phase velocity value at the corresponding period given on top of each map. Hatched polygons indicate the tectonic features drawn after Fig. 1.

Figure S5. Isotropic (top) Rayleigh and (bottom) Love wave phase velocity maps at periods of 22, 25 and 30 s. Phase velocity perturbations are plotted relative to a regional average phase velocity value at the corresponding period given on top of each map. Hatched polygons indicate the tectonic features drawn after Fig. 1.

Please note: Oxford University Press is not responsible for the content or functionality of any supporting materials supplied by the authors. Any queries (other than missing material) should be directed to the corresponding author for the paper.